1   # Submesoscale Hotspots of Productivity and Respiration: Insights

2   # from High-Resolution Oxygen and Fluorescence Sections

3

4   Rachel H. R. Stanley[1]*, Dennis J. McGillicuddy, Jr.[2], Zoe O. Sandwith[2], and Haley M. Pleskow[1]

5   [1] Wellesley College, 106 Central St. Wellesley, MA 02480

6   [2] Woods Hole Oceanographic Institution, 360 Woods Hole Rd., Woods Hole, MA USA 02543

7

8   * corresponding author: rachel.stanley@wellesley.edu, 001-781-283-3122

9

ABSTRACT: Modeling studies have shown that mesoscale and submesoscale processes can stimulate phytoplankton productivity and export production. Here, we present observations from an undulating, towed Video Plankton Recorder (VPR-II) in the tropical Atlantic. The VPR-II collected profiles of oxygen, fluorescence, temperature and salinity in the upper 140 m of the water column at a spatial resolution of 1 m in the vertical and <2 km in the horizontal. The data reveal remarkable "hotspots", i.e. locations 5 to 10 km wide which have elevated fluorescence and decreased oxygen, both of which are likely the result of intense submesoscale upwelling. Based on estimates of source water, estimated from identical temperature and salinity surfaces, hotspots are more often areas of net respiration than areas of net production — although the inferred changes in oxygen are subject to uncertainty in the determination of the source of the upwelled waters since the true source water may not have been sampled. We discuss the spatial distribution of these hotspots and present a conceptual model outlining their possible generation and decline. Simultaneous measurements of O_2/Ar in the mixed layer from a shipboard mass spectrometer provide estimates of rates of surface net community production. We find that the subsurface biological hotspots are often expressed as an increase in mixed layer rates of net community production. Overall, the large number of these hotspots support the growing evidence that submesoscale processes are important drivers in upper ocean biological production.

Keywords: Net Community Production, photosynthesis, respiration, oxygen, fluorescence, patchiness, hotspots, O_2/Ar

Highlights:

- Submesoscale hotspots are found in upper ocean sections of oxygen and fluorescence
- Apparent changes in oxygen within the hotspots are sometimes negative
- This may reflect increased respiration or errors in inference of source water

1

2   -   Hotspots are linked to mixed layer increases in net community production

3

4   **1. Introduction**

5   The mechanisms responsible for seasonal accumulation of oxygen within the euphotic zone

6   in the oligotrophic waters of the open ocean (Jenkins and Goldman, 1985; Shulenberger and

7   Reid, 1981) remain enigmatic. Both observations and models have suggested that episodic

8   processes such as eddies and fronts play a role in providing nutrients to fuel upper ocean

9   productivity (Falkowski *et al.*, 1991; Klein and Lapeyre, 2009; Lévy *et al.*, 2001; Mahadevan

10   and Archer, 2000; McGillicuddy, 2016; McGillicuddy *et al.*, 2007; Oschlies, 2002) and to

11   increase carbon export (Omand *et al.*, 2015). In particular, numerical studies have shown that

12   episodic upwelling, associated with submesoscale fronts (Klein and Lapeyre, 2009; Lévy *et al.*,

13   2001), may be able to provide nutrients required for phytoplankton growth (Lévy *et al.*, 2012a;

14   Lévy *et al.*, 2012b) and consequently may result in patches of biological production (Brody *et*

15   *al.*, 2016; Mahadevan, 2016; Resplandy *et al.*, 2012).

16   Observational work has illustrated submesoscale variations in many of the parameters

17   associated with biological production (i.e. fluorescence, community structure, etc.), though

18   studies of direct variations in rates of production are much fewer. In particular, filamentous

19   patterns in chlorophyll encircling an eddy have been observed from remote sensing that mimic

20   patterns in sea surface temp and align with sea surface altimetry (Calil and Richards, 2010).

21   Spectral analysis of high resolution chlorophyll data has usually shown more variability in in

22   chlorophyll than in temperature (Hodges and Rudnick, 2006; Mahadevan and Campbell, 2002).

1   While chlorophyll is one of the best studied parameters, perhaps because of its detectability with

2   remote sensing, high resolution sampling of other biologically relevant variables has occurred.

3   For example, a high resolution spatial survey based on fast rate repetition fluoremetry showed

4   intensified phytoplankton activity near fronts (Guidi *et al.*, 2012). Patchiness has also been

5   shown in community structure through high resolution flow cytometry studies (Martin *et al.*,

6   2005; Martin *et al.*, 2008; Martin *et al.*, 2010). Additionally, rates of net community production

7   and export production have been measured on the submesoscale through O_2/Ar ratios and high

8   resolution ^{234}Th (Estapa *et al.*, 2015).

9   New observational approaches using autonomous profiling floats and gliders have provided

10   insight into the biogeochemical dynamics of episodic processes (Johnson *et al.*, 2010;

11   Mahadevan *et al.*, 2012; Nicholson *et al.*, 2008), but thus far the space-time coverage of such

12   deployments has not been sufficient to fully characterize these phenomena. Here we utilize

13   towed undulating instrumentation to obtain synoptic cross-sections of physical and

14   biogeochemical properties in the upper ocean. These data provide a detailed view into the

15   structure of mesoscale and submesoscale fluctuations in fluorescence and oxygen, from which

16   inferences can be made about net community production (NCP).

17   Both towed vehicles and gliders are extremely useful for gaining information on the

18   mesoscale and submesoscale (Rudnick, 2016). It is important to note, however, that towed

19   vehicles can resolve much shorter temporal and smaller spatial scales than gliders, owing to the

20   greater speed at which they move through the water (Rudnick and Cole, 2011). In particular,

21   instrumentation can be towed an order of magnitude faster than gliders and thus offer a

22   "snapshot" of the ocean state which allows them to be used to assess submesoscale spatial

23   variability. For example, in the data presented here, one transect consisting of 438 profiles to

1   140 m depth and covering 300 km was completed in 19 hours. In contrast, in a study by

2   Nicholson et al. (2015), the gliders sampled in a bowtie pattern over a 50 km x 50 km square for

3   3.5 months and completed 14 profiles to 700 m every 24 hours. The slower speed of gliders

4   makes it difficult to separate spatial and temporal variability, with gliders more often being used

5   to assess temporal variability (Damerell *et al.*, 2016; Nicholson *et al.*, 2015) than spatial. Other

6   differences include that gliders can persist in the water for much longer than towed vehicles

7   which allows them to give very useful pictures of temporal evolution. Gliders typically sample

8   deeper in the water column (to 700 or 1000 m) than towed vehicles (140 m in the case of the

9   Video Plankton Recorder II and 500 m in the case of SeaSoar II). Both gliders and towed

10   vehicles can be outfitted with biogeochemical sensors such as those for fluorescence, oxygen,

11   and nitrate, yielding detailed views of variations in net community production (Biddle *et al.*,

12   2015; Damerell *et al.*, 2016; Nicholson *et al.*, 2015; Pidcock *et al.*, 2010).

13   Changes in oxygen concentration can be used to quantify rates of photosynthesis and

14   respiration. Photosynthesis produces oxygen and respiration consumes it and thus the net change

15   in oxygen reflects the net amount of photosynthesis and respiration, i.e. NCP. However, oxygen

16   is also affected by physical processes such as mixing and gas exchange, with the saturation state

17   of oxygen being dependent on temperature and to a lesser degree, salinity. In the mixed layer,

18   argon (Ar) is often used as an abiotic analogue for oxygen since it has similar physicochemical

19   characteristics. Thus, the ratio of O_2/Ar (Emerson *et al.*, 1991) or the difference between the

20   saturation states of O_2 and Ar (Craig and Hayward, 1987; Spitzer and Jenkins, 1989), can be

21   used in a steady state model and combined with estimates of diffusive gas exchange to calculate

22   mixed layer NCP (e.g. Hendricks *et al.*, 2004; Juranek and Quay, 2005; Reuer *et al.*, 2007). At

23   depths between the base of the mixed layer and the euphotic zone, a time series of O_2/Ar

1 measurements can be used to calculated NCP. Below the euphotic zone, Ar is not as useful as an

2 analogue for O_2, since Ar profiles with depth are often different than those of O_2; O_2 declines

3 sharply below the euphotic zone due to remineralization, but Ar changes much less.

4 Additionally, Ar is less useful since gas exchange does not directly affect the water below the

5 mixed layer. O_2 concentration alone can be used to quantify rates of net community production if

6 there is some independent "clock" – either a water mass being followed for a certain amount of

7 time (Riser and Johnson, 2008) or a tracer age calculated (Stanley *et al.*, 2012). If there is no

8 clock, as in the case of the data presented here, then exact rates cannot be calculated but the sign

9 of NCP can be inferred by the difference of the O_2 concentration compared to the apparent

10 source waters, i.e. net photosynthesis or net respiration.

11 In this work, we used the Video Plankton Recorder II (VPR-II), a towed undulating

12 instrument (Davis *et al.*, 2005), to collect profiles of oxygen, fluorescence, temperature and

13 salinity in the upper 140 m of the subtropical and tropical Atlantic Ocean at roughly 2 km

14 horizontal resolution. In section 2, we describe the data collection and analysis. In section 3, we

15 present results showing that hotspots can be seen in the O_2 and fluorescence records. These are

16 regions, usually a few km in width and ten meters or so in depth, that have elevated fluorescence

17 and usually decreased oxygen concentrations compared to the water at the same depth. The

18 decrease in oxygen could be a signature of the source water for these events (i.e. upwelled

19 oxygen debt) or could be a result of increased respiration over photosynthetic production and

20 thus could be reflecting negative NCP. We also present a statistical analysis of the hotspot

21 distribution, including the decorrelation length scales in the vertical and horizontal directions,

22 and a conceptual model of hotspot evolution. We furthermore link the subsurface hotspots to

1   surface expressions of rates of net community production, which tend to be positive in the

2   overlying waters within the mixed layer.

3

2. Methods

2.1.   Cruise Description

6   Data for this research were collected on the R/V *Oceanus* (Voyage #471) in the subtropical

7   and tropical Atlantic (12ºN and 32ºN and 53ºW to 66.5ºW, see Fig. 1 for cruise-track) between

8   April 25, 2011 and May 13, 2011. Eddy features were targeted through the use of real-time

9   altimetric data (Leben *et al.*, 2002), supplemented by data from shipboard acoustic Doppler

10   current profiler (ADCP), expendable bathythermographs (XBT) and the VPR-II. Retrospective

11   analysis of the shipboard observations was carried out in the context of Absolute Dynamic

12   Topography (ADT) from AVISO (http://www.aviso.oceanobs.com) , which is the sum of sea

13   level anomaly (SLA) and mean dynamic topography (Rio *et al.*, 2011). ADT is more appropriate

14   than SLA for defining the eddy field in areas of significant mean currents, insofar as fluctuations

15   in the mean flow can be expressed as mesoscale variations in SLA.

16   Fifteen VPR-II tows (Fig. 1), most of which were 300 to 400 km in length, were

17   completed throughout the cruise. The initial and final latitude and longitude of each tow are

18   listed in Supplementary Table S1. Before each VPR-II tow, a conductivity, temperature, depth

19   (CTD) rosette was lowered to allow for collection of water for chemical and biological analysis.

20   Data from the cruise, including all the VPR data, are archived at the biological-chemical

21   oceanography data-management office (BCO-DMO) under project 2104:

22   http://www.bco-dmo.org/project/2104 .

23

2.2. Profiles from the VPR-II

The VPR-II (Davis *et al.*, 2005) undulated between the surface and typically 140 m depth and collected 6 to 7 profiles of a suite of physical and biogeochemical parameters every 10 km. The average ship speed was 10 knots and the average VPR vertical velocity was 1 m s^{-1}. The horizontal resolution of the VPR-II along the cruise-track was 1.5 km, as measured between the shallowest depth (~5 m) of two adjacent profiles (or 0.75 km if comparing up-cast and down-cast profiles instead of two up-cast profiles). The resolution along the towtrack was centimeters to meters, depending on the response time of the sensors. Data were collected in 1 sec averages and then were averaged into 1 m bins to facilitate analysis of the suite of variables on a common grid. Between 30 m and the surface, the VPR-II flew off to the side of the ship in order to avoid the ship's wake (Davis *et al.*, 2005). The VPR-II contained numerous sensors. The Video Plankton Recorder (VPR) itself is an underwater video system that yields a continuous record of plankton and seston abundance and community structure (Davis *et al.*, 2004; Davis *et al.*, 2005; Hu and Davis, 2005). However, the VPR does not yield estimates of phytoplankton biomass because only the larger size classes (e.g. diatoms) are detected in the optical imagery. A CTD gave detailed characterization of the physical properties of temperature, salinity, and thus by extension density.

Measurements from a fluorometer onboard the VPR provided a proxy for chlorophyll *a* concentration, reported here in relative fluorescence units (RFU). Factory calibrations were used in processing the fluorometer data to obtain an estimated chlorophyll a concentration. Conversion to of these estimates into quantitatively accurate chlorophyll a concentrations for this particular oceanographic regime would require additional calibration with in situ pigment measurements, which were not collected during this expedition.

1   A Seabird SBE-43 oxygen sensor was incorporated into the VPR-II system in order to obtain

2   detailed O_2 profiles. The SBE-43 O_2 sensor has a short enough response time (2 s) to be able to

3   accurately profile O_2 as the VPR-II undulates. However, the sensor is known to drift. Pre- and

4   post- factory calibrations, performed in June 2010 and June 2011, of the SBE-43 sensor showed

5   that the measured O_2 from the SBE-43 sensor differed by on average 0.66 μM at the surface and

6   0.01 μM O_2 at 150 dbar depth depending on whether the pre-cruise or post-cruise calibration was

7   used. The precision of the SBE43, based on other studies, is 1 μmol kg^{-1} (Coppola *et al.*, 2013).

8   The intake and plumbing configuration delivering water to the SBE43, as well as a

9   mismatch between the computer system and GPS time, introduced a temporal offset between the

10   sensor's output voltage and the corresponding measurements of temperature and salinity, with

11   the combined temporal offset ranging from 0.4 to 2.9 seconds depending on the VPR tow. This

12   time constant was inferred by minimizing the sum of the squared differences in resultant oxygen

13   concentrations at the same depth on adjacent profiles of the VPR (i.e. the "up-cast" compared to

14   the "down-cast").

15   Profiles of fluorescence and oxygen in the upper ocean contain strong mean gradients that

16   can obscure the submesoscale structures of primary interest in this study. Fluorescence (F') and

17   oxygen anomalies (O_2') were therefore derived for each tow by subtracting from the data the

18   depth averaged mean value of F or O_2 computed for 1 dbar depth bins (n ~ 450, depending on the

19   tow). When fluorescence and O_2 anomalies are calculated with respect to density contours rather

20   than depth ones, the conclusions of this paper remain the same. We present anomalies based on

21   depth rather than density in the figures of this paper because light is a function of depth rather

22   than density and light is one of the main controls on fluorescence.

1   *2.3.   Quantitative Criterion for Hotspots*

2   In order to examine the distribution of hotspots with longitude, latitude, and depth, we

3   identified the hotspots by first noting the locations where there was either a (i) greater than 3.5

4   standard deviation change in oxygen concentration anomaly or (ii) a greater than 3.5 standard

5   deviation change in fluorescence anomaly concurrent with a fluorescence signal of greater than

6   0.03 rfu. The results did not change much if we defined a hotspot as having at least a 4 standard

7   deviation anomaly or a 3 standard deviation anomaly. We only considered depths between 20 m

8   and 100 m in the above method for finding hotspots in order to avoid the upper water column

9   where the fluorescence signal is quenched (on the shallow end) and to avoid finding hotspots

10   solely associated with the subsurface chlorophyll maximum (on the deep end). Hotspot locations

11   were confirmed by eye – scattered data points that met the considerations but were not located

12   near other data points that met the criteria were not classified as hotspots (such as numerous

13   points between 20 m and 50 m in VPR transect 4 , Fig. S4 for example). Additionally, data

14   points that appeared to be solely associated with the subsurface chlorophyll maximum were not

15   classified as hotspots. Specifically, 558 data points met the >3.5 standard deviation criterions

16   with the data points grouping in 96 distinct hot spots. Of these, 51 hotspots were confirmed

17   visually using the additional criteria described above. All hotspots determined from these

18   criterion are circled in the supplemental figures (Fig. S1-S14) and locations of all those hotspots

19   appear on Fig. 1 and 2. However, since the latitude/longitude of some of those hotspots is very

20   similar to each other, they sometimes appear as one circle on Fig. 1, resulting in fewer hotspots

21   noted on Fig. 1 than appear in Fig. S1 to S14.

22   *2.4.   Mixed layer O_2/Ar Record*

1   For the second half of the cruise, i.e. starting at VPR-II tow 9, an equilibrator inlet mass

2   spectrometer (EIMS) onboard the ship quantified O_2/Ar continuously in water collected from the

3   ship's underway flow-through system (nominal depth of 3 m), thereby revealing concentrations

4   of mixed layer O_2/Ar simultaneously with the VPR-II tows. The EIMS followed the design of

5   Cassar et al. (2009), and included a Pfeiffer Prismaplus Quadrupole mounted to a Varian

6   Turboplus pumping station. Equilibration of gas with the underway water was achieved through

7   the use of Liqui-cel Micromodule cartridges, which have an equilibration time scale of several

8   minutes. The system was calibrated every 4 to 6 hours during the cruise by measuring air, which

9   has a constant O_2/Ar ratio (Hamme *et al.*, 2012). Additionally, samples were collected from the

10   underway system into custom-made, evacuated, pre-poisoned glass sample bottles (Emerson *et*

11   *al.*, 1991), and were analyzed after the cruise for O_2/Ar on an isotope ratio mass spectrometer,

12   according to the method of Barkan and Luz (2003). Samples simultaneously collected from

13   Niskins on the CTD rosette and the underway water showed no systematic offset, confirming

14   respiration was not occurring in the ship's flow-through water system.

15   Rates of mixed layer net community production were calculated from the O_2/Ar data, in

16   units of mmol O_2 m^{-2} d^{-1}, according to the equation:

17

18                         $NCP = k\, \rho\, [O_2]_{sat}\, \Delta(O_2/Ar)$ (1)

19

20   where k is the gas transfer velocity, ρ is the density of water as calculated by Millero and Poisson

21   (1981), $[O_2]_{sat}$ is the equilibrium concentration of oxygen at the temperature and salinity of the

22   sample (Garcia and Gordon, 1992) in units of mmol kg^{-1}, and $\Delta(O_2/Ar)$ is the biological

23   superaturation. $\Delta(O_2/Ar)$ is thus defined as $(O_2/Ar)_{meas}/(O_2/Ar)_{eq} -1$, where the subscript *meas*

refers to the O_2/Ar gas ratio measured by the EIMS and the subscript *eq* refers to the gas ratio at

solubility equilibrium. Ar solubilities were calculated using the relationship with temperature and

salinity determined by Hamme and Emerson (2004). The gas transfer velocity was calculated

using the Stanley et al. (2009) gas exchange parameterization, with a 60 day weighted average

applied (Reuer *et al.*, 2007). This method for calculating NCP from continuous mixed layer

O_2/Ar ratios has been used extensively in the last few years (Cassar *et al.*, 2011; Hamme *et al.*,

2012; Juranek *et al.*, 2012; Lockwood *et al.*, 2012; Stanley *et al.*, 2010). An atmospheric pressure

of 1 atm was assumed when calculating $O_{2,sat}$ introducing an error of approximately 2%: the

actual atmospheric pressure was 1.019 ± 0.006 atm. The major uncertainties in calculating of

NCP result from entrainment of O_2 from below the mixed layer (Jonsson *et al.*, 2013) and from

uncertainties in the air-sea gas exchange parameterization. Since the purpose of the NCP in this

data is mainly qualitative – i.e. showing that increases in NCP are collocated with hotspots –

corrections for entrainment of O_2 were not included for all transects. However, such corrections

were estimated using profiles of O from the VPR and from the CTD casts to be less than 20% of

NCP most of the time. Corrections were larger during some hotspots due to larger negative O_2

gradients and thus corrected records showed even more pronounced peaks in NCP at hotspot

locations than the estimates given in this paper (since lack of correction means an underestimate

of NCP at the hotspot).

3. Results and Discussion

3.1.   Description of Hotspots

Data from an example VPR tow, tow #9, is presented in Fig. 2. Data from the other tows are

presented in Supplemental Figs. S1 to S14. We discuss VPR tow #9 as a case study - similar

1   interpretations are made with the other tows (Supplementary Figs S1 to S14, Table 1). In tow #9,

2   several hotspots can clearly be observed as large anomalies in the fluorescence record (Fig. 2e).

3   For example, strong hotspots occur at approximately 150 km, 190 km, and 280 to 320 km.

4   Weaker hotspots occur at numerous other places, such as at 170 km and 210 km. The hotspots

5   can be seen in the O_2 anomaly record (Fig. 2f) as areas where low O_2 water is penetrating

6   upwards; usually, the hotspots appear at the upper end of these plumes of low O_2 water. The

7   upwelled water can be seen as having a slightly lower potential temperature (Fig. 2a) and a

8   barely distinguishable change in salinity (Fig. 2b). Unfortunately, we only have a two-

9   dimensional slice through these hotspots – we do not see their three-dimensional structure or

10   how they are evolving in space or time from this dataset. As such, inference of continuity in the

11   observed property distributions is risky—although we refer to the high-fluorescence low-oxygen

12   water as having been upwelled, its trajectory is by no means constrained to the two-dimensional

13   transect we measured.

14   In this particular transect (VPR #9), water from the Amazon river plume is apparent, as

15   evidenced by the lens of low salinity water near the surface. Hotspots are seen as deeper water

16   penetrates upward into this lens of low salinity water. This low salinity water is not present in all

17   the transects (see Supplemental Figs. S1 to S14).

18

19   *3.2.   Hotspot Distribution with Location and Depth*

20   Locations of hotspots found by this method, marked by dots on Fig. 1, reveal that the

21   hotspots are ubiquitous but not evenly distributed along the tows. Rather they cluster, with a

22   number of hotspots appearing in a short stretch, followed by a gap sometimes as large as

1   hundreds of kilometers, and then another cluster of hotspots. The hotspots are not preferentially

2   associated with either cyclonic or anticyclonic eddies. The hotspots seem to be preferentially

3   associated with crossing edges of eddies (fronts), though it is difficult to tell for certain since the

4   cruise track crosses so many eddies and not all crossings have hotspots. We quantitatively

5   examined a possible link between hotspot location and gradient of sea height anomaly by

6   correlating hotspot abundance with the gradient in satellite-based ADT. We found that in the

7   northern section of the cruise (i.e. Fig. 1 a, north of 19°N), there was no preference for hotspots

8   to occur at larger gradients of ADT. In contrast, in the southern section of the cruise (Fig. 1b),

9   there is a higher proportion of hotspots at large ADT gradients (Fig. 3) than at small ADT

10   gradients. In particular, the *number* of hotspots is uniform as a function of ADT gradient (Fig.

11   3a) even though there are many fewer locations with high ADT gradients (Fig. 3b). Thus, the

12   *fraction* of hotspots relative to the number of locations with a certain ADT gradient shows that

13   there are preferentially more hotspots at higher ADT gradients (Fig. 3c) in the southern section.

14   The hotspots are evenly distributed throughout all depths between 20 and 100 m (depths

15   considered in the analysis). There was no discernible pattern in location of hotspots with depth

16   either in a given tow or as a function of latitude. Analysis of vertical decorrelation length scales

17   shows in general shorter length scales for fluorescence and sometimes for oxygen than for

18   temperature, suggesting that the hotspots are likely indeed a result of biological activity rather

19   than simply physical transport (supplemental Fig. S15, supplemental material text). However, the

20   differences are not statistically significant and the decorrelation length scales are likely reflecting

21   properties of the water both inside and outside the hotspots.

22

1   *3.3.   Change in oxygen within hotspots*

2   The hotspots we identified almost always have a lower oxygen concentration than the

3   surrounding water at the same depth (Fig. S1– S14). This in part is due to upwelled oxygen debt,

4   which could be enhanced by respiration or reduced by photosynthesis along the trajectory of the

5   water parcel. In order to quantify the net change in oxygen, one needs to know the initial oxygen

6   concentration prior to upwelling. Unfortunately, our data are on only single transects through

7   three-dimensional fields that are evolving in time. Therefore, we cannot definitively identify the

8   source waters for each hotspot. However, we can make a crude estimate of the source water

9   oxygen concentration by calculating the average O_2 in water with the same density, T, and S

10   properties deeper in the water column and within 100 km of the hotspot ($[O_2]_{T,S}$; see Fig. 4 for an

11   example, using VPR tow #9 as a case study. We use the tighter constraint of similar temperature

12   and salinity, rather than just density, in order to obtain a better estimate of the source water. We

13   calculated the difference between the average oxygen within the hotspot ($[O_2]_{hotspot}$) and the

14   average oxygen in water with the temperature and salinity within one standard deviation of the

15   average temperature and salinity of water within the hotspot: $\Delta[O_2]=[O_2]_{hotspot} - [O_2]_{T,S}$. If $\Delta[O_2]$

16   is positive, it represents a net gain of oxygen in the hotspot, and thus likely net production, in

17   spite of the apparent decrease in O_2 when simply comparing the hotspot directly to water at the

18   same depth. If $\Delta[O_2]$ is negative, then net respiration is likely happening within the hotspot. A

19   conceptual model explaining a possible pathway for net production and net respiration is

20   discussed below (Section 3.4).

21   It is of course possible that the water with the same T/S properties along the transect is not

22   necessarily the source water for the hotspot. Indeed, ADCP data along the cruise track (Fig. S16)

23   suggests that in the case of the hotspot in Fig. 4, the real source water may be off the track and to

15

1   the west-southwest of the hotspot, rather than along the track. In particular, the ADCP data

2   suggest ENE flow at the hotspot itself and NW flow at the potential source water at x=200. The

3   sense of the flow is qualitatively consistent with the altimetric map (Fig. 1), suggesting

4   connectivity of these features via meandering of the periphery of an anticyclonic eddy. Ideally,

5   one would map the three-dimensional structure and follow the evolution of a hotspot in time to

6   see if net respiration or net production was occurring. However, in the absence of such data, this

7   method gives a very rough idea of whether net production or net respiration is occurring, i.e. if

8   the hotspot is net heterotrophic or net autotrophic.

9   In spite of these uncertainties in source water, Table 1 lists ΔO_2, $O_{2\_hotspot}$, and $O_{2\_T,S}$,

10   with standard errors, for the hotspots most easily identified by eye, assuming the source waters

11   are indeed on the transect. Since the table only lists a subset of the hotspots, , i.e. the major

12   hotspots, for which we chose to conduct the ΔO_2 analysis, there are more hotspots circled in the

13   supplementary figures (S1to S14) than are in Table 1. Nonetheless, all hotspots listed in Table 1

14   can be matched to circled hotspots in the supplementary figure (Fig. S1 to S14) by the tow

15   number, distances, and depths given in the table. Standard deviation is reported as well, in order

16   to illustrate the variability in the oxygen concentrations; however, standard error is a better

17   estimate of the uncertainty in the mean O_2 in the hotspot which is ultimately what we need to

18   compare to the mean O_2 outside the hotspot. The average euphotic zone depth over the transects

19   is 103 m (standard deviation = 21 m).

20   ΔO_2 is negative in approximately two-thirds of the hotspots; it is positive in the remaining

21   one-third, reflecting that the hotspots are likely more often locations of net respiration rather than

22   net production (if the assumptions about source water are correct – otherwise, the ΔO_2 may be a

1   reflection of source waters that are not on the tow). However, the changes are often small with

2   ΔO_2 being close to the standard error of its components. We performed t-tests to statistically

3   determine if the differences in O_2 between inside the hotspot and outside it are significant and in

4   all cases, the difference is significant to at least the 95% confidence level – in most cases, it is

5   significant to greater than 99% confidence. We also calculated ΔO_2 based on the bottom and top

6   quartiles of O_2 concentration as an alternative way to calculating it based on mean O_2

7   concentrations. The conclusions about which hotspots were positive and negative and also that

8   the differences are significant between hotspots and surrounding waters remained the same with

9   the quartile analysis as with the mean analysis.

10   The symbols on Fig. 1 are color-coded according to whether the hotspot was one of net

11   production (green), net respiration (red), or not considered in this analysis because it was a

12   smaller hotspot (blue). One can see from the figure that there is no discernible pattern of likely

13   net respiration (negative ΔO_2) or likely net photosynthesis (positive ΔO_2) with latitude or

14   longitude or with location with respect to eddy features.

15   From Table 1, it is clear that the question of net change in oxygen, perhaps surprisingly, is

16   not intimately tied to depth – there are shallow hotspots with negative ΔO_2 and deeper ones with

17   positive ΔO_2. Also, there are times when hotspots of positive ΔO_2 and negative ΔO_2 are right

18   next to each other – in some cases (tow 11, ~40 km into the tow; Supplemental Fig. S10) the

19   bottom of a wide hotspot has net respiration whereas the top has net production. In other cases

20   (tow 16, ~250 to 285 km into the tow; Supplemental Fig. S14), the first of a series of three

21   hotspots has positive ΔO_2 and thus likely net production and then the second and third hotspots,

22   which are shallower, have negative ΔO_2 and thus likely net respiration. If future work confirms

17

1   that some hotspots are truly negative (rather than the result being an artefact of the estimate of

2   source water), it would be important to understand why some hotspots seem to have net

3   production and others net respiration- a focused study on the temporal evolution of hotspots

4   could answer that question. It also would be interesting to know not just the net effect of

5   photosynthesis and respiration but also the rates of those processes separately. Independent

6   estimates of rates of photosynthesis from gas tracer techniques such as triple oxygen isotopes or

7   bottle incubations, and of rates of respiration from tritiated thymidine incubations or other

8   techniques would be very useful in this context.

9   We converted ΔO_2 to a rate in oxygen production by assuming that the hotspot evolved

10   over one to ten days (Lévy *et al.*, 2012a). This is a very rough estimate but gives an order of

11   magnitude idea of the rates of net community production within the hotspot. The rates range

12   from -18 mmol O_2 m^{-3} d^{-1} to 10 mmol O_2 m^{-3} d^{-1} if a time-scale of one day is used and a range of

13   -2 mmol O_2 m^{-3} d^{-1} to 1 mmol O_2 m^{-3} d^{-1} if a time-scale of ten days is used. For comparison, rates

14   of net primary production (which equals net community production plus heterotrophic

15   respiration and thus a likely upper maximum on average rates of production) in the subtropical

16   North Atlantic are 0.6 to 1.2 mmol O_2 m^{-3} d^{-1} (assuming a photosynthetic quotient of 1.2)

17   (Lomas *et al.*, 2013; Saba *et al.*, 2010). Rates of bacterial production are estimated at 0.1 to 0.6

18   mmol O_2 m^{-3} d^{-1} (Lomas *et al.*, 2013). Rates of net community production in the subtropical

19   North Atlantic are typically 0.1 to 0.3 mmol O_2 m^{-3} d^{-1} (Brix *et al.*, 2006; Gruber, 1998; Spitzer

20   and Jenkins, 1989; Stanley *et al.*, 2012). When compared to prior estimates of NCP for the

21   region (0.1 – 0.3 mmol O_2 m^{-3} d^{-1}), the highest rates of oxygen accumulation we infer from our

22   data (1 – 10 mmol O_2 m^{-3} d^{-1}) are (3,10,30,100) times larger, depending on whether upper or

23   lower bounds are used for each. Of course, the potential burst of production and respiration

1   within a hotspot is likely different from the seasonal or annual average production and

2   respiration rates that were assessed in the above studies. The fact that the changes estimated for

3   these hotspots are 3, 10, 30 or 100 times larger than average measured production and respiration

4   in the region suggests that bursts of production and respiration could account for the observed

5   changes in O_2. In contrast, the O_2 decreases observed in the hotspots are orders of magnitude too

6   large to likely be explained by increased respiration of dissolved organic carbon (DOC) that

7   could potentially be upwelled during the hotspot formation event – remineralization of semilabile

8   DOC is estimated at 0.004 to 0.03 mmol O_2 m^{-3} d^{-1} (Carlson *et al.*, 2010; Hansell, 2013) which is

9   two to three orders of magnitude smaller than the changes inferred for the hotspots in which

10   oxygen decreases.

11

12   *3.4.   Conceptual Model*

13   In order to interpret the observed hotspots, we have formulated a conceptual model of

14   nutrient (N), new production (NP), respiration (R), fluorescence (F), and oxygen (O) anomalies

15   that result along the Lagrangian trajectory of a submesoscale upwelling event (Fig. 5a). We have

16   formulated this model from first principles, based on expected autotrophic responses for vertical

17   motion and thus it explains the positive ΔO_2 hotspots. Of course we do not expect exact

18   correspondence between the idealized model and the observed hotspots (Table 1) that are taking

19   place in a fully three-dimensional turbulent fluid. However, the systematic discrepancies

20   between them shed light on shortcomings of this conceptual framework. After presenting the

21   idealized model, we discuss which assumptions must change to account for the surprisingly more

22   common negative ΔO_2 hotspots. In particular, the negative ΔO_2 hotspots have two possible

1   explanations: (1) source waters that are different than the transect (see section 3.3) and thus

2   where negative ΔO_2 is not inconsistent with the idealized, autotrophic conceptual model first

3   presented or (2) enhanced respiration within the hotspots, a scenario that requires some

4   modification of the conceptual model, which is shown in the rightmost two columns of Fig. 5a.

5   The conceptual model describes several stages. Stage I reflects the pre-upwelling conditions

6   below the euphotic zone, in which nutrients are in abundance, oxygen is low, and light is

7   insufficient for NCP (NP and F both at background). As the water parcel upwells (Stage II),

8   nutrients are introduced into the euphotic zone which stimulates new production and respiration,

9   increasing both fluorescence and oxygen—but there are subtleties in the two latter aspects: (1)

10   the fluorescence anomaly is enhanced by the high chlorophyll:carbon ratio characteristic of

11   phytoplankton inhabiting the low-light conditions of the base of the euphotic zone (e.g. Cullen,

12   1982); and (2) although the oxygen content of the water parcel increases as a result of new

13   production, it is still low in oxygen relative to surrounding waters; the oxygen anomaly has

14   simply become less negative. As the parcel continues to upwell (Stage III), higher light

15   conditions stimulate more new production, removing nutrients and increasing oxygen. The

16   higher light environment accommodates lower chlorophyll:carbon ratios, thereby lessening the

17   fluorescence anomaly. As the upwelled nutrients become exhausted (Stage IV), new production

18   and fluorescence return to background levels, with the positive oxygen anomaly providing the

19   only detectable biogeochemical signature of the submesoscale upwelling event.

20   A complication arises in the interpretation of the conceptual model if there is downwelling

21   rather than upwelling (Fig. 5b). In the presence of a subsurface fluorescence maximum,

22   downwelling produces adjacent anomalies of opposite sign. When coupled with the associated

23   anomalies in oxygen, this introduces a new category of perturbation which we refer to as Stage

V: a negative fluorescence anomaly together with a positive oxygen anomaly. Further

complicating matters, the interval a little deeper consists of a positive fluorescence anomaly in

combination with a positive oxygen anomaly, which is indistinguishable from Stage III in the

upwelling case.

The stages of the conceptual model can be observed by examining concurrent changes in

O_2' and F' (where the prime notations refer to the anomalies defined in section 2.2)(Fig. 5c). We

observed all five stages in our data, though not all tows show the full range of stages. In

particular, the hotspots are almost always stage II. In many cases, we can observe stage I water

progressing to stage II in a vertical sense (Fig. 6, around 200 km and again around 300 km); i.e.

stage II water overlying stage I water, with the location of the stage II water being the same

location we identified as a hotspot from fluorescence and oxygen. However, this may be

misleading because fluid trajectories are not constrained to the two-dimensional transects we

measured. Interestingly, we rarely find stage III water overlying stage II water, even though in

the conceptual model one would expect such a progression. Again, this may be due to the three-

dimensional nature of the phenomenology.

The observation mentioned in Section 3.3 that the oxygen concentration in the hotspots is

usually decreasing, even after an attempt to take into account the upwelled oxygen debt, suggests

that the conceptual model presented above may need some modification. One possibility is that

an increase in zooplankton activity, perhaps due to active migration to the hotspots, could

explain the increase in respiration that we infer. We do not see any linkage between whether

hotspots are positive or negative and time of day; however our sampling was biased toward

nighttime, so it is difficult to assess the potential connection between oxygen debts observed in

the hotspots and diel vertical migration by zooplankton.

1   Another possibility is that as the water upwells, the heterotrophic microbial population may

2   be responding more strongly to the vertical change than the autotrophs. This is hard to

3   understand, especially in shallower waters were the upwelling would be concurrent with a large

4   increase in light which would favor the autotrophs. However, support for the speculation that

5   heterotrophs may be responding more strongly or quickly than autotrophs comes from evidence

6   that heterotrophs have been shown to have a synchronous and rapid response to high frequency

7   variability by turning on certain genes, especially those for growth and nutrient acquisition

8   (Ottesen *et al.*, 2013). Thus a variant of the conceptual model which would explain the negative

9   O_2 anomaly hot spots would be to increase the strength of the heterotrophic respiration R term as

10   the water rises. Thus the positive O_2 anomalies near the surface could become negative,

11   reflecting what is observed in many of the hotspots. This scenario is presented in the rightmost

12   two columns of Fig. 5a.

13   Unfortunately, the data collected in this study are not sufficient to unequivocally determine

14   whether hotspots truly have negative NCP nor to explain why negative NCP is observed in

15   hotspots. As discussed above, the apparently negative NCP may be a result of source waters not

16   on the transect and thus the conceptual model may not need to include those lasts two columns.

17   Independent estimates of rates of photosynthesis and respiration within the hotspots – as well as

18   information on the source water and how the hotspots evolve in time – are necessary.

19

20   *3.5.   Relationship to mixed layer Net Community Production rates*

21   Although the data we have precludes calculation of rates of productivity within the hotspots

22   themselves (other than the very crude estimates presented in Section 3.3), we are able to estimate

1   rates of net community production in the mixed layer above the hotspots from continuous O_2/Ar

2   data collected from the underway system using an at-sea mass spectrometer for VPR tows 9 to

3   16. We have not accounted for mixing or entrainment when calculating the NCP (see section 2.4)

4   and thus these estimates can have errors of $\sim 20\%$ (with that number based on corrections

5   estimated from the vertical gradient in oxygen). Including entrainment corrections would make

6   the calculated NCP be larger at the hotspots and thus would reinforce the conclusion that

7   hotspots are usually associated with increases in NCP. We examined the records of NCP for

8   correspondence with the locations of the subsurface hotspots. We find that in 62% of the

9   hotspots on tows VPR 9 through VPR 16 (the tows for which we have concurrent O_2/Ar data),

10   the subsurface hotspots are expressed in the mixed layer as increases in NCP. For 24% of the

11   cases, the hotspots are expressed as depressions in NCP – this is usually in hotspots deeper than

12   50 m and may be a result of entrainment of low O_2 water that was not included in our

13   calculations of NCP. In the remaining 14% of the cases, there is no change in NCP at the hotspot

14   location – this is often the case for the hotspots that are only a few km wide.

15   For example, in VPR tow #9, the three hotspots that are most obvious to the eye are all

16   expressed as peaks in the mixed layer NCP record (peaks at ~150, 180 and 300 km in Fig. 7).

17   One less pronounced (i.e. smaller anomaly in fluorescence), deeper hotspot (stage 2 at 65 m

18   located at ~215km in Fig. 2) also appears as a peak in mixed layer NCP (peak at ~215 km in Fig.

19   7). There also is an overall depression in NCP in the area of the elongated hotspot (280 to 320

20   km in Fig 7) that may be due to upward mixing of the low O_2 water associated with the hotspot

21   (Fig. 2d) contaminating the surface NCP calculation. Interestingly, even the hotspots that appear

22   to have negative NCP at depth from the crude source water analysis (section 3.3), often appear as

23   local increases in NCP in the mixed layer above the hotspot. Thus the peaks we see in the NCP

23

1   record are not simply a result of transport of O_2 from the thermocline hotspots – if they were, we

2   would be seeing depressions in the NCP record rather than elevations. Instead, the peaks in the

3   NCP records are likely real signs of increased values of net community production at the same

4   locations as the thermocline hotspots. This suggests that while many of the hotspots may initially

5   have low O_2 concentrations compared to surrounding waters, as the water parcel rises, the

6   combination of influx of O_2 from gas exchange and O_2 from increased photosynthesis in the

7   hotspot, results in the hot spots being expressed as high O_2 concentration at the surface.

8   Additionally, the correspondence of peaks in continuous records of NCP with subsurface

9   hotspots is significant because in many locations of the ocean, such peaks in NCP have been

10   observed without the high-resolution subsurface information necessary to characterize the

11   processes involved (Lockwood *et al.*, 2012; Stanley *et al.*, 2010; Ulfsbo *et al.*, 2014). Now we

12   can see that least for this cruise, many of the peaks in surface NCP are related to variability in

13   production and respiration at depth.

14   Other peaks appear in the NCP record that do not correspond to locations of hotspots found

15   by the VPR-II. These may be remnants of hotspots from previous events – the gas tracer method

16   averages over several days to weeks whereas the VPR-II tow gave us a snapshot of fluorescence

17   and oxygen anomalies. Alternatively, those peaks may be related to features that are not aligned

18   with our two-dimensional transects, and thus the three-dimensionality precludes making direct

19   connections with the causal upwelling cells. Lastly, the peaks in NCP may reflect mixed layer

20   processes not at all related to the subsurface hotspot activity. A further discussion of the

21   intricacies and implications of the mixed layer O_2/Ar record and resultant mixed layer NCP

22   estimates is beyond the scope of this paper. Overall, these findings highlight the necessity of

24

making a four-dimensional study of the hotspots to better learn how primary productivity and respiration changes within the hotspots and in the mixed layer above them.

4. Conclusions

In summary, high-resolution (<1 km spacing) profiles of O_2 and fluorescence from an undulating, towed instrument reveal that hotspots are prevalent. The hotspots are not predictably distributed by latitude or longitude, by depth in the water column, or by position with reference to cyclonic or anticyclonic eddies. The hotspots in almost all cases have decreased O_2 compared to the surrounding water. This is likely due, at least in part, to upwelled oxygen debt. However, even when taking this upwelled debt into account by examining the difference in O_2 from likely source water (water with same T, S), many of the hotspots show a decrease in O_2. This surprisingly suggests that in the hotspots, there often is increased respiration over photosynthesis, resulting in negative NCP. However, without a mapping of the hotspots in three dimensions and time, we cannot be sure what is the source water for the hotspots and thus some of the seemingly negative changes in O_2 could be explained by advection of water parcels with lower oxygen concentrations. A conceptual model, based on current oceanographic paradigms, was presented that can explain hotspots that show an increase in O_2 relative to the surrounding water; revisions to the conceptual model are suggested to explain the hypothesized simulation of respiration within hotspots. The hotspots, even though they occur at depth and often with a decrease in O_2, are often associated with increased rates of NCP in the mixed layer at the same locations. Again, fully four-dimensional surveys are needed to resolve the connections between NCP in the mixed layer and the processes below.

The high-resolution data presented here is intriguing evidence of biological hotspots. Small scale variations such as these have been predicted in models (Mahadevan, 2016). If these hotspots do indeed have substantially different NCP than the surrounding water, then they could lead to significant changes in our estimates of NCP in the upper ocean and could support modeling work that shows that submeoscale physical processes are crucial for setting biological productivity in the upper ocean. Given the small spatial and short temporal scales of these hotspots, characterizing them from an observational perspective remains a challenge. The two-dimensional cross-sections presented herein provide a window into their variability, but full four-dimensional (space and time) surveys are sorely needed.

Much work remains to be done. Rates of photosynthesis and respiration, measured within the hotspots, are crucial for determining if hotspots are truly regions of negative NCP. Mechanisms for hotspot evolution have yet to be determined. Community structure of both autotrophs and heterotrophs within the hotspots is not known. A four-dimensional survey of the hotspots with adaptive sampling and high-resolution numerical modeling are essential in order to better understand the nature and significance of these hotspots.

5. Acknowledgements

6

7. References

8   Barkan, E., Luz, B., 2003. High-precision measurements of O-17/O-16 and O-18/O-16 of O-2 and O-2/Ar
9   ratio in air. Rapid Communications in Mass Spectrometry 17 (24), 2809-2814.
10 Biddle, L.C., Kaiser, J., Heywood, K.J., Thompson, A.F., Jenkins, A., 2015. Ocean glider observations of
11 iceberg-enhanced biological production in the northwestern Weddell Sea. Geophysical Research Letters
12 42 (2), 459-465.
13 Brix, H., Gruber, N., Karl, D.M., Bates, N.R., 2006. On the relationships between primary, net community,
14 and export production in subtropical gyres. Deep-Sea Research Part Ii-Topical Studies in Oceanography
15 53 (5-7), 698-717.
16 Brody, S.R., Lozier, M.S., Mahadevan, A., 2016. Quantifying the impact of submesoscale processes on the
17 spring phytoplankton bloom in a turbulent upper ocean using a Lagrangian approach. Geophysical
18 Research Letters 43 (10), 5160-5169.
19 Calil, P.H.R., Richards, K.J., 2010. Transient upwelling hot spots in the oligotrophic North Pacific. Journal
20 of Geophysical Research-Oceans 115.
21 Carlson, C.A., Hansell, D.A., Nelson, N.B., Siegel, D.A., Smethie, W.M., Khatiwala, S., Meyers, M.M.,
22 Halewood, E., 2010. Dissolved organic carbon export and subsequent remineralization in the
23 mesopelagic and bathypelagic realms of the North Atlantic basin. Deep-Sea Research Part Ii-Topical
24 Studies in Oceanography 57 (16), 1433-1445.
25 Cassar, N., Barnett, B.A., Bender, M.L., Kaiser, J., Hamme, R.C., Tilbrook, B., 2009. Continuous High-
26 Frequency Dissolved O-2/Ar Measurements by Equilibrator Inlet Mass Spectrometry. Analytical
27 Chemistry 81 (5), 1855-1864.
28 Cassar, N., DiFiore, P.J., Barnett, B.A., Bender, M.L., Bowie, A.R., Tilbrook, B., Petrou, K., Westwood, K.J.,
29 Wright, S.W., Lefevre, D., 2011. The influence of iron and light on net community production in the
30 Subantarctic and Polar Frontal Zones. Biogeosciences 8, 227-237.
31 Coppola, L., Salvetat, F., Delauney, L., Machoczek, D., Karstensen, J., Sparnocchia, S., Thierry, V., Hydes,
32 D., Haller, M., Nair, R., 2013. White Paper on Dissolved Oxygen Measurements: Scientific Needs and
33 Sensors Accuracy. Jerico Project: Scientific Needs and Sensors Accuracy. Ifremer, Brest, France.
34 Craig, H., Hayward, T., 1987. Oxygen supersaturation in the ocean: biological versus physical
35 contributions. Science 235, 199-202.
36 Cullen, J.J., 1982. The deep chlorophyll maximum: comparing vertical profiles of chlorophyll a. Canadian
37 Journal Fish Aquatic Science 39, 791-803.

Damerell, G.M., Heywood, K.J., Thompson, A.F., Binetti, U., Kaiser, J., 2016. The vertical structure of upper ocean variability at the Porcupine Abyssal Plain during 2012-2013. Journal of Geophysical Research-Oceans 121 (5), 3075-3089.

Davis, C.S., Hu, Q., Gallager, S.M., Tang, X., Ashjian, C.J., 2004. Real-time observation of taxa-specific plankton distributions: an optical sampling method. Marine Ecology-Progress Series 284, 77-96.

Davis, C.S., Thwaites, F.T., Gallager, S.M., Hu, Q., 2005. A three-axis fast-tow digital Video Plankton Recorder for rapid surveys of plankton taxa and hydrography. Limnology and Oceanography-Methods 3, 59-74.

Emerson, S., Quay, P., Stump, C., Wilbur, D., Knox, M., 1991. O2, Ar, N2, and 222Rn in surface waters of the subarctic ocean: Net biological O2 Production. Global Biogeochemical Cycles 5, 49-69.

Estapa, M.L., Siegel, D.A., Buesseler, K.O., Stanley, R.H.R., Lomas, M.W., Nelson, N.B., 2015. Decoupling of net community and export production on submesoscales in the Sargasso Sea. Global Biogeochem. Cycles 29, 1266-1282.

Falkowski, P.G., Ziemann, D., Kolber, Z., Bienfang, P.K., 1991. Role of eddy pumping in enhancing primary production in the ocean. Nature 352, 55-58.

Garcia, H.E., Gordon, L.I., 1992. Oxygen solubility in water: better fitting equations. Limnology and Oceanography 37 (6), 1307-1312.

Gruber, N., 1998. Anthropogenic CO2 in the Atlantic Ocean. Global Biogeochemical Cycles 12 (1), 165-191.

Guidi, L., Calil, P.H.R., Duhamel, S., Bjorkman, K.M., Doney, S.C., Jackson, G.A., Li, B.L., Church, M.J., Tozzi, S., Kolber, Z.S., Richards, K.J., Fong, A.A., Letelier, R.M., Gorsky, G., Stemmann, L., Karl, D.M., 2012. Does eddy-eddy interaction control surface phytoplankton distribution and carbon export in the North Pacific Subtropical Gyre? Journal of Geophysical Research-Biogeosciences 117.

Hamme, R.C., Cassar, N., Lance, V.P., Vaillancourt, R.D., Bender, M.L., Strutton, P.G., Moore, T.S., DeGrandpre, M.D., Sabine, C.L., Ho, D.T., Hargreaves, B.R., 2012. Dissolved O2/Ar and other methods reveal rapid changes in productivity during a Lagrangian experiment in the Southern Ocean. Journal of Geophysical Research-Oceans 117, C00F12.

Hamme, R.C., Emerson, S., 2004. The solubility of neon, nitrogen and argon in distilled water and seawater. Deep Sea Research I 51 (11), 1517-1528.

Hansell, D.A., 2013. Recalcitrant Dissolved Organic Carbon Fractions. Annual Review of Marine Science, Vol 5 5, 421-445.

Hendricks, M.B., Bender, M.L., Barnett, B.A., 2004. Net and gross O-2 production in the Southern Ocean from measurements of biological O-2 saturation and its triple isotope composition. Deep-Sea Research Part I-Oceanographic Research Papers 51 (11), 1541-1561.

Hodges, B.A., Rudnick, D.L., 2006. Horizontal variability in chlorophyll fluorescence and potential temperature. Deep-Sea Research Part I-Oceanographic Research Papers 53 (9), 1460-1482.

Hu, Q., Davis, C., 2005. Automatic plankton image recognition with co-occurrence matrices and Support Vector Machine. Marine Ecology-Progress Series 295, 21-31.

Jenkins, W.J., Goldman, J., 1985. Seasonal oxygen cycling and primary production in the Sargasso Sea. Journal of Marine Research 43, 465-491.

Johnson, K.S., Riser, S.C., Karl, D.M., 2010. Nitrate supply from deep to near-surface waters of the North Pacific subtropical gyre. Nature 465 (7301), 1062-1065.

Jonsson, B.F., Doney, S.C., Dunne, J., Bender, M., 2013. Evaluation of the Southern Ocean O2/Ar-based NCP estimates in a model framework. Journal of Geophysical Research: Biogeosciences 118 (2), 385-399.

Juranek, L.W., Quay, P.D., 2005. In vitro and in situ gross primary and net community production in the North Pacific Subtropical Gyre using labeled and natural abundance isotopes of dissolved O-2. Global Biogeochemical Cycles 19 (3), doi:10.1029/2004GB002384.

Juranek, L.W., Quay, P.D., Feely, R.A., Lockwood, D., Karl, D.M., Church, M.J., 2012. Biological production in the NE Pacific and its influence on air-sea CO2 flux: Evidence from dissolved oxygen isotopes and O2/Ar. Journal of Geophysical Research-Oceans (117).

Klein, P., Lapeyre, G., 2009. The Oceanic Vertical Pump Induced by Mesoscale and Submesoscale Turbulence. Annual Review of Marine Science 1, 351-375.

Leben, R.R., Born, G.H., Engebreth, B.R., 2002. Operational altimeter data processing for mesoscale monitoring. Marine Geodesy 25, 3-18.

Lévy, M., Ferrari, R., Franks, P.J.S., Martin, A.P., Riviere, P., 2012a. Bringing physics to life at the submesoscale. Geophysical Research Letters 39.

Lévy, M., Iovino, D., Resplandy, L., Klein, P., Madec, G., Treguier, A.M., Masson, S., Takahashi, K., 2012b. Large-scale impacts of submesoscale dynamics on phytoplankton: Local and remote effects. Ocean Modelling 43-44, 77-93.

Lévy, M., Klein, P., Treguier, A.M., 2001. Impact of sub-mesoscale physics on production and subduction of phytoplankton in an oligotrophic regime. Journal of Marine Research 59 (4), 535-565.

Lockwood, D., Quay, P.D., Kavanaugh, M.T., Juranek, L.W., Feely, R.A., 2012. High-resolution estimates of net community production and air-sea CO2 flux in the northeast Pacific. Global Biogeochemical Cycles 26.

Lomas, M.W., Bates, N.R., Johnson, R.J., Knap, A.H., Steinberg, D.K., Carlson, C.A., 2013. Two decades and counting: 24-years of sustained open ocean biogeochemical measurements in the Sargasso Sea. Deep-Sea Research Part Ii-Topical Studies in Oceanography 93, 16-32.

Mahadevan, A., 2016. The Impact of Submesoscale Physics on Primary Productivity of Plankton. In: Carlson, C.A., Giovannoni, S.J. (Eds.), Annual Review of Marine Science, Vol 8. Annual Reviews, Palo Alto, pp. 161-184.

Mahadevan, A., Archer, D., 2000. Modeling the impact of fronts and mesoscale circulation on the nutrient supply and biogeochemistry of the upper ocean. J. Geophys. Res. 105, 1209-1225.

Mahadevan, A., Campbell, J.W., 2002. Biogeochemical patchiness at the sea surface. Geophysical Research Letters 29 (19), doi:10.1029/2001GL014116.

Mahadevan, A., D'Asaro, E., Lee, C., Perry, M.J., 2012. Eddy-Driven Stratification Initiates North Atlantic Spring Phytoplankton Blooms. Science 337 (6090), 54-58.

Martin, A.P., Zubkov, M.V., Burkill, P.H., Holland, R.J., 2005. Extreme spatial variability in marine picoplankton and its consequences for interpreting Eulerian time-series. Biology Letters 1 (3), 366-369.

Martin, A.P., Zubkov, M.V., Fasham, M.J., Burkill, P.H., Holland, R.J., 2008. Microbial spatial variability: An example from the Celtic Sea. Progress in Oceanography 76 (4), 443-465.

Martin, A.P., Zubkov, M.V., Holland, R.J., Tarran, G., Burkill, P., 2010. Variability in ultraplankton at the Porcupine Abyssal Plain study site. Deep-Sea Research Part Ii-Topical Studies in Oceanography 57 (15), 1336-1345.

McGillicuddy, D.J., 2016. Mechanisms of Physical-Biological-Biogeochemical Interaction at the Oceanic Mesoscale. In: Carlson, C.A., Giovannoni, S.J. (Eds.), Annual Review of Marine Science, Vol 8. Annual Reviews, Palo Alto, pp. 125-+.

McGillicuddy, D.J., Anderson, L.A., Bates, N.R., Bibby, T., Buesseler, K.O., Carlson, C.A., Davis, C.S., Ewart, C., Falkowski, P.G., Goldthwait, S.A., Hansell, D.A., Jenkins, W.J., Johnson, R., Kosnyrev, V.K., Ledwell, J.R., Li, Q.P., Siegel, D.A., Steinberg, D.K., 2007. Eddy/wind interactions stimulate extraordinary mid-ocean plankton blooms. Science 316, 1021-1026.

Millero, F.J., Poisson, A., 1981. International One-Atmosphere Equation of State of Seawater. Deep-Sea Research Part a-Oceanographic Research Papers 28 (6), 625-629.

Nicholson, D., Emerson, S., Eriksen, C.C., 2008. Net community production in the deep euphotic zone of the subtropical North Pacific gyre from glider surveys. Limnology & Oceanography 53 (5(2)), 2226-2236.

Nicholson, D.P., Wilson, S.T., Doney, S.C., Karl, D.M., 2015. Quantifying subtropical North Pacific gyre mixed layer primary productivity from Seaglider observations of diel oxygen cycles. Geophysical Research Letters 42 (10), 4032-4039.

Omand, M.M., D'Asaro, E.A., Lee, C.M., Perry, M.J., Briggs, N., Cetinic, I., Mahadevan, A., 2015. Eddy-driven subduction exports particulate organic carbon from the spring bloom. Science 348 (6231), 222-225.

Oschlies, A., 2002. Can eddies make ocean deserts bloom? Global Biogeochem. Cycles 16 (4), 1106.

Ottesen, E.A., Young, C.R., Eppley, J.M., Ryan, J.P., Chavez, F.P., Scholin, C.A., DeLong, E.F., 2013. Pattern and synchrony of gene expression among sympatric marine microbial populations. Proceedings of the National Academy of Sciences of the United States of America 110 (6), E488-E497.

Pidcock, R., Srokosz, M., Allen, J., Hartman, M., Painter, S., Mowlem, M., Hydes, D., Martin, A., 2010. A Novel Integration of an Ultraviolet Nitrate Sensor On Board a Towed Vehicle for Mapping Open-Ocean Submesoscale Nitrate Variability. Journal of Atmospheric and Oceanic Technology 27 (8), 1410-1416.

Resplandy, L., Martin, A.P., Le Moigne, F., Martin, P., Aquilina, A., Memery, L., Levy, M., Sanders, R., 2012. How does dynamical spatial variability impact 234Th-derived estimates of organic export? Deep Sea Research I 68, 24-45.

Reuer, M.K., Barnett, B.A., Bender, M.L., Falkowski, P.G., Hendricks, M.B., 2007. New estimates of Southern Ocean biological production rates from O-2/Ar ratios and the triple isotope composition of O-2. Deep-Sea Research Part I-Oceanographic Research Papers 54 (6), 951-974.

Rio, M.H., Guinehut, S., Larnicol, G., 2011. New CNES-CLS09 global mean dynamic topography computed from the combination of GRACE data, altimetry, and in situ measurements. Journal of Geophysical Research-Oceans 116.

Riser, S.C., Johnson, K.S., 2008. Net production of oxygen in the subtropical ocean. Nature 451 (7176), 323-U325.

Rudnick, D.L., 2016. Ocean Research Enabled by Underwater Gliders. In: Carlson, C.A., Giovannoni, S.J. (Eds.), Annual Review of Marine Science, Vol 8. Annual Reviews, Palo Alto, pp. 519-+.

Rudnick, D.L., Cole, S.T., 2011. On sampling the ocean using underwater gliders. Journal of Geophysical Research-Oceans 116.

Saba, V.S., Friedrichs, M.A.M., Carr, M.E., Antoine, D., Armstrong, R.A., Asanuma, I., Aumont, O., Bates, N.R., Behrenfeld, M.J., Bennington, V., Bopp, L., Bruggeman, J., Buitenhuis, E.T., Church, M.J., Ciotti, A.M., Doney, S.C., Dowell, M., Dunne, J., Dutkiewicz, S., Gregg, W., Hoepffner, N., Hyde, K.J.W., Ishizaka, J., Kameda, T., Karl, D.M., Lima, I., Lomas, M.W., Marra, J., McKinley, G.A., Melin, F., Moore, J.K., Morel, A., O'Reilly, J., Salihoglu, B., Scardi, M., Smyth, T.J., Tang, S.L., Tjiputra, J., Uitz, J., Vichi, M., Waters, K., Westberry, T.K., Yool, A., 2010. Challenges of modeling depth-integrated marine primary productivity over multiple decades: A case study at BATS and HOT. Global Biogeochemical Cycles 24.

Shulenberger, E., Reid, J.L., 1981. The Pacific shallow oxygen maximum, deep chlorophyll maximum, and primary productivity, reconsidered. Deep-Sea Res. 28A, 901-919.

Spitzer, W.S., Jenkins, W.J., 1989. Rates of vertical mixing, gas-exchange and new production - estimates from seasonal gas cycles in the upper ocean near Bermuda. Journal of Marine Research 47 (1), 169-196.

Stanley, R.H.R., Doney, S.C., Jenkins, W.J., Lott III, D.E., 2012. Apparent oxygen utilization rates calculated from tritium and helium-3 profiles at the Bermuda Atlantic Time-series Study site. Biogeosciences doi:10.5194/bg-9-1969-2012, 9977-10015.

Stanley, R.H.R., Jenkins, W.J., Doney, S.C., Lott III, D.E., 2009. Noble Gas Constraints on Air-Sea Gas Exchange and Bubble Fluxes. Journal of Geophysical Research - Oceans 114, doi:10.1029/2009JC005396.

Stanley, R.H.R., Kirkpatrick, J.B., Barnett, B., Cassar, N., Bender, M.L., 2010. Net community production and gross production rates in the Western Equatorial Pacific. Global Biogeochemical Cycles 24, GB4001, doi:4010.1029/2009GB003651.

1   Ulfsbo, A., Cassar, N., Korhonen, M., van Heuven, S., Hoppema, M., Kattner, G., Anderson, L.G., 2014.
2   Late summernet community production in the central Arctic Ocean using multiple approaches. Global
3   Biogeochemical Cycles 28 (10), 1129-1148.

4

5

Table 1. For hotspots with the along-tow distance and depth range listed, the mean O_2 concentration ($\mu mol\ L^{-1}$) within the hotspot as well as the mean O_2 on the same temperature and salinity surface is used to calculate the change in O_2 (ΔO_2). That change is converted to a rate assuming time-scale of a hotspot feature to be 1 or 10 days. Bold rows denote rows where the change in oxygen is negative, implying increased respiration within the hotspot.

| VPR tow	Along-tow distance (km)	Depth (m)	In Hot Spot			On same T, S surface			$\Delta[O_2]$			Rate for t=1 d (mmol m^{-3} d^{-1})	Rate for t=10 d (mmol m^{-3} d^{-1})
			Mean [O₂] (μM)	Std dev [O₂] (μM)	Std err [O₂] (μM)	Mean [O₂] (μM)	Std dev [O₂] (μM)	Std err [O₂] (μM)	Δ[O₂] (μmol L⁻¹)	Std dev propagated	Std error propagated		
1	**598-604**	**90-100**	**190.55**	**4.3**	**0.5**	**201.0**	**8.5**	**2.1**	**-10.4**	**9.5**	**2.2**	**-10.6**	**-1.1**
2	233-239	75-85	198.8	3.0	0.4	198.6	2.4	0.2	0.2	3.8	0.4	0.2	0.0
3	155-159	85-90	195.2	1.1	0.2	195.0	0.8	0.1	0.2	1.4	0.2	0.2	0.0
3	250-256	32-35	204.94	0.9	0.2	204.5	0.6	0.0	0.5	1.0	0.2	0.5	0.0
3	**258-260**	**65-70**	**201.87**	**2.2**	**0.6**	**203.6**	**1.5**	**0.0**	**-1.8**	**2.7**	**0.6**	**-1.8**	**-0.2**
5	**105-110**	**55-65**	**197.88**	**4.0**	**0.4**	**206.8**	**0.4**	**0.1**	**-9.0**	**4.0**	**0.4**	**-9.1**	**-0.9**
5	**110-120**	**70-80**	**190.65**	**4.6**	**0.4**	**201.3**	**1.7**	**0.2**	**-10.6**	**4.9**	**0.5**	**-10.8**	**-1.1**
5	**110-120**	**85-95**	**196.05**	**1.8**	**0.2**	**196.7**	**2.1**	**0.1**	**-0.6**	**2.8**	**0.2**	**-0.6**	**-0.1**
6	152-155	40-50	194.72	1.9	0.4	185.2	3.6	0.2	9.6	4.1	0.4	9.7	1.0
6	155-160	50-60	187.51	4.0	0.5	179.3	0.8	0.1	8.2	4.1	0.5	8.3	0.8
6	**270-272**	**56-62**	**171.99**	**0.8**	**0.2**	**172.6**	**1.3**	**0.3**	**-0.6**	**1.5**	**0.4**	**-0.6**	**-0.1**
6	278-281	58-62	179.31	4.7	1.2	176.7	5.7	1.5	2.6	7.4	1.9	2.7	0.3
7	**143-146**	**20-35**	**195.69**	**0.3**	**0.0**	**196.8**	**0.5**	**0.1**	**-1.1**	**0.6**	**0.1**	**-1.1**	**-0.1**
7	**143-146**	**45-55**	**194.98**	**0.4**	**0.1**	**196.4**	**0.3**	**0.0**	**-1.4**	**0.5**	**0.1**	**-1.4**	**-0.1**
7	286-291	64-70	192.86	1.4	0.2	191.6	4.2	0.6	1.3	4.4	0.6	1.3	0.1
8	**19-22**	**78-84**	**197.26**	**3.0**	**0.7**	**200.4**	**2.1**	**0.2**	**-3.1**	**3.6**	**0.7**	**-3.1**	**-0.3**
9	**147-152**	**21-26**	**186.3**	**4.5**	**0.8**	**187.9**	**2.6**	**0.7**	**-1.5**	**5.2**	**1.1**	**-1.5**	**-0.2**
9	**188-192**	**20-28**	**182.7**	**5.0**	**0.7**	**188.5**	**5.2**	**0.5**	**-5.8**	**7.2**	**0.9**	**-5.9**	**-0.6**
9	**288-292**	**35-42**	**150.1**	**1.7**	**0.3**	**152.7**	**4.6**	**0.4**	**-2.6**	**4.9**	**0.5**	**-2.6**	**-0.3**
11	43-53	15-20	200.8	0.6	0.1	199.6	0.7	0.0	1.1	1.0	0.1	1.1	0.1
11	**45-50**	**52-60**	**203.6**	**0.2**	**0.0**	**204.2**	**0.2**	**0.0**	**-0.6**	**0.3**	**0.0**	**-0.6**	**-0.1**
12	**110-113**	**70-80**	**198.8**	**1.7**	**0.3**	**199.7**	**2.0**	**0.1**	**-0.9**	**2.6**	**0.3**	**-0.9**	**-0.1**
12	110-113	80-90	202.6	1.4	0.2	198.4	2.2	0.1	4.3	2.6	0.3	4.3	0.4
15	247-252	60-65	203.0	2.1	0.4	200.8	3.6	0.4	2.2	4.2	0.5	2.2	0.2
16	**53-58**	**90-94**	**193.1**	**0.4**	**0.1**	**193.7**	**0.9**	**0.1**	**-0.5**	**1.0**	**0.1**	**-0.6**	**-0.1**
16	249-252	45-55	194.5	1.0	0.2	192.2	3.7	0.2	2.3	3.8	0.3	2.4	0.2
16	**260-270**	**36-44**	**186.4**	**2.6**	**0.2**	**188.0**	**9.4**	**0.6**	**-1.5**	**9.8**	**0.7**	**-1.6**	**-0.2**
16	**285-288**	**36-44**	**191.4**	**3.3**	**0.6**	**197.1**	**3.8**	**0.4**	**-5.7**	**5.1**	**0.7**	**-5.8**	**-0.6**

1

2

Figure 1

3
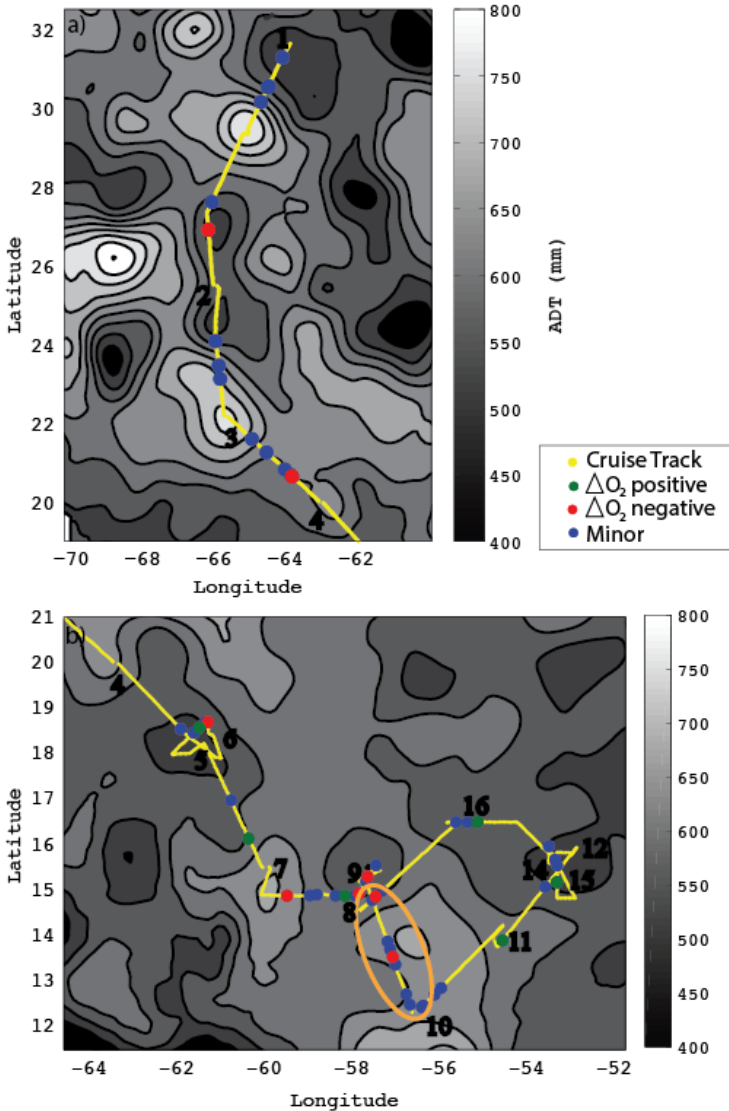
Fig. 1. Locations of VPR II tows, illustrating the cruise track, overlain on absolute dynamic topography (ADT), with contours at 50 mm intervals. The cruise track is split into two segments to facilitate higher resolution and to better match the satellite altimetry with the timing of the cruise segments (April 27 for upper panel and May 11 for lower panel). Locations of submesoscale hotspots identified in the data are indicated by dots, with green dots indicating major hotspots where the inferred ΔO_2 is positive, and red dots indicating major hotspots where ΔO_2 is negative (see text). Blue dots represent minor hotspots, i.e. those with smaller anomalies in O_2 and fluorescence. The orange oval denotes the location of VPR transect 9, which is shown in detail in Figure 2. Black numbers depict the starting location of each VPR transect.

1
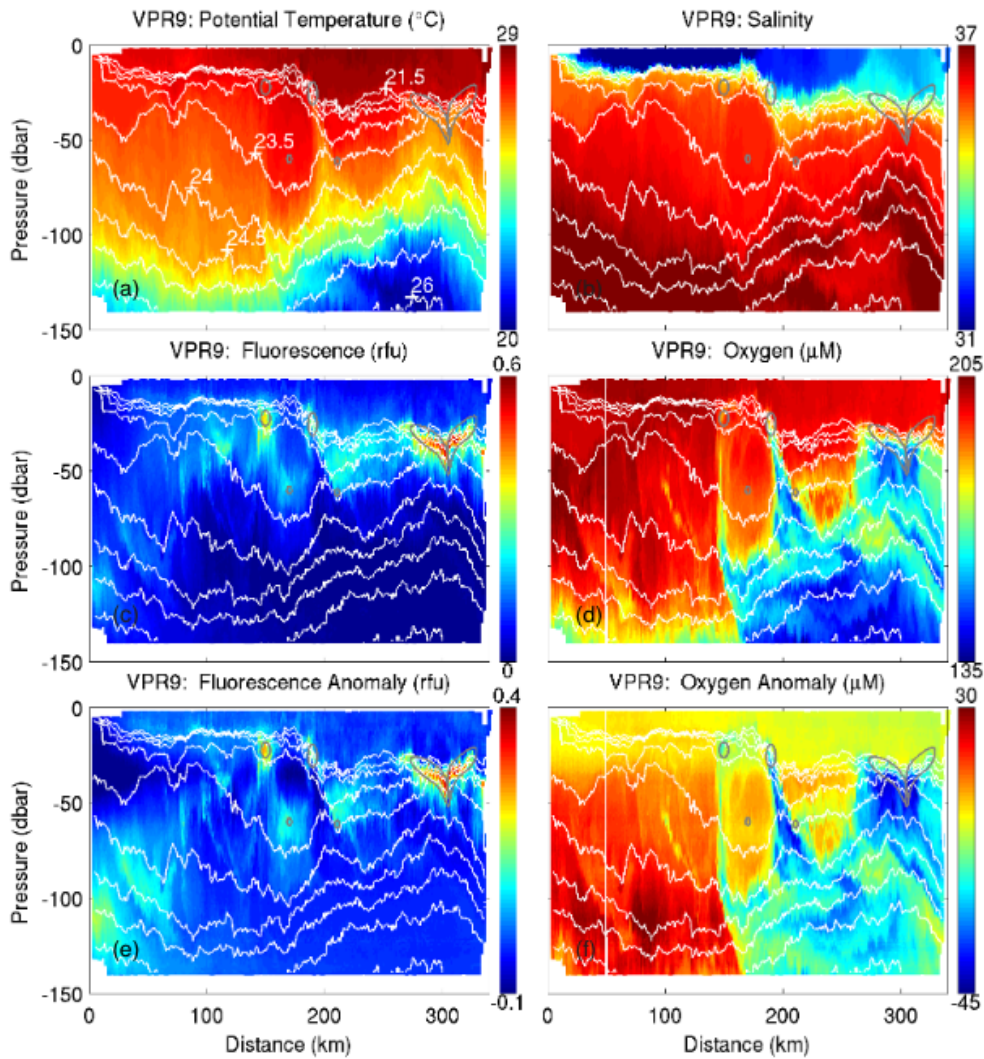
Fig. 2. Data from VPR tow #9: (a) potential temperature in deg C, (b) salinity (c) fluorescence (relative fluorescent units), (d) oxygen concentration in μmol L^{-1}, (e) fluorescence anomaly (relative fluorescence units), and (f) oxygen concentration anomaly in units of μmol L^{-1}. The labels next to the color bar reflect the minimum and maximum values of that property on this tow. The gray circles reflect the location of the hotspots marked in Fig. 1. White lines represent isopycnal surfaces. Data are not contoured – rather each pixel represents a data point collected by sensors on the VPR-II. Data for the other VPR transects are in the supplemental figures S1 to S14.
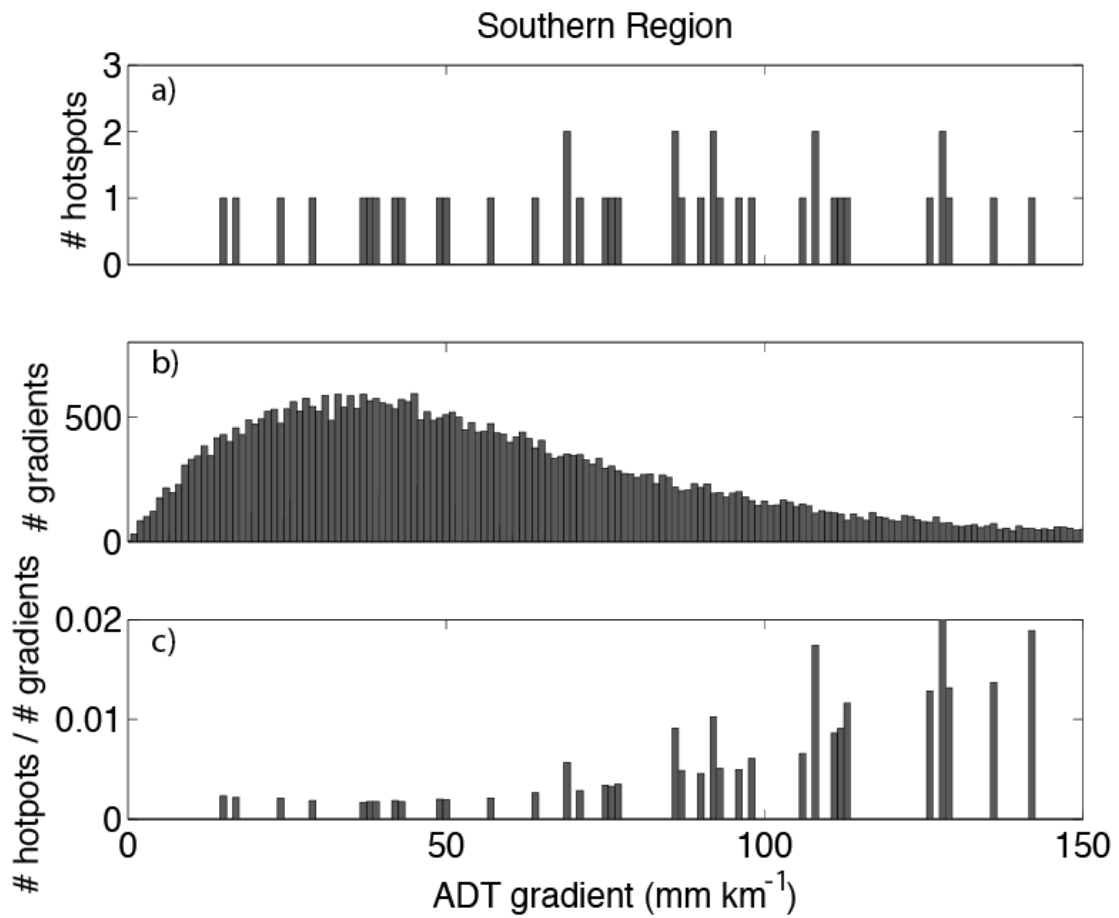
Figure 3

Fig. 3. (a) Histogram of the number of hotspots (see text for details on definition of hotspot) with respect to gradient in absolute dynamic topography (ADT) for the southern section of the cruise (latitude < 21 °N) . (b) Histogram of the number of gradients in ADT found during the southern section of cruise track in order to give perspective on the probability of finding a given gradient in ADT. (c) The quotient of number of hotspots divided by number of gradients shows that hotspots are more likely to occur at larger gradients of ADT.

1
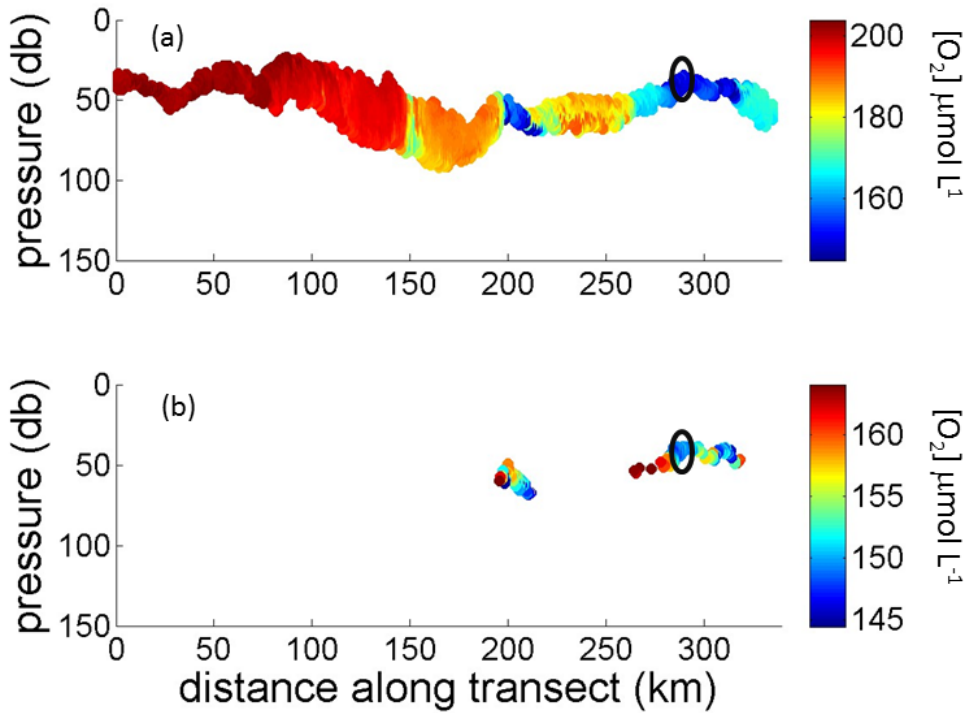
Fig. 4. Oxygen concentration (μmol L^{-1}) along (a) a constant density surface and (b) a constant
temperature and salinity surface (T=26.32 °C, S=35.77 psu) chosen to match that of the hotspot
located at approximately 300 km (circled in black) on VPR transect #9 (Fig. 2). Note that the
oxygen concentration within the hotspot is on average lower than other oxygen concentrations on
the same temperature/salinity surface. Thus the calculated change in oxygen (ΔO_2) is negative
for this hotspot, suggesting negative NCP and hence excess of respiration over photosynthesis.
However, uncertainties remain on whether water with the same temperature and salinity is truly
the source water for the hotspot since the source water could have come from water not on the
transect path.

(a)   Conceptual Model

Surface Mixed Layer				positive NCP hotspot		negative NCP hotspot	
Stage IV	N^{bg}	NP^{bg}	F^{bg}	O^{+}	R^{bg}	O^{+}	R^{bg}
Stage III	N^{+}	NP^{++}	F^{+}	O^{bg}	R^{bg}	O^{-}	R^{+}
Stage II	N^{++}	NP^{+}	F^{++}	O^{-}	R^{bg}	O^{--}	R^{+}
Stage I	N^{++}	NP^{bg}	F^{bg}	O^{--}	R^{bg}	O^{--}	R^{bg}
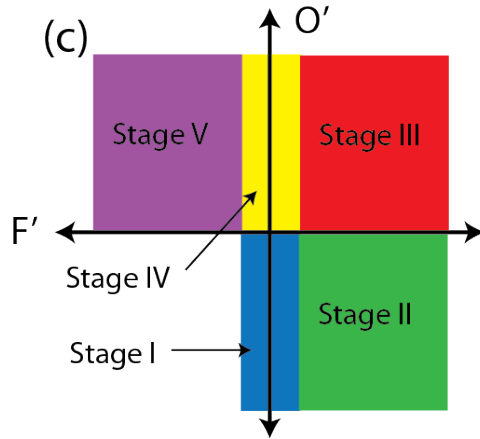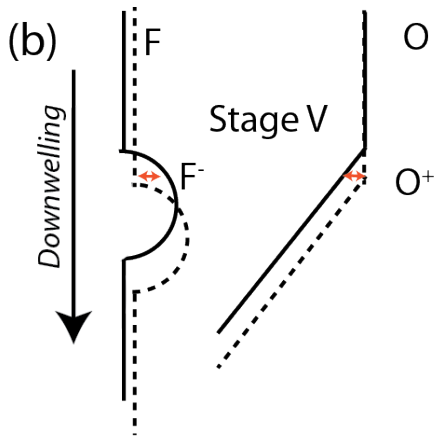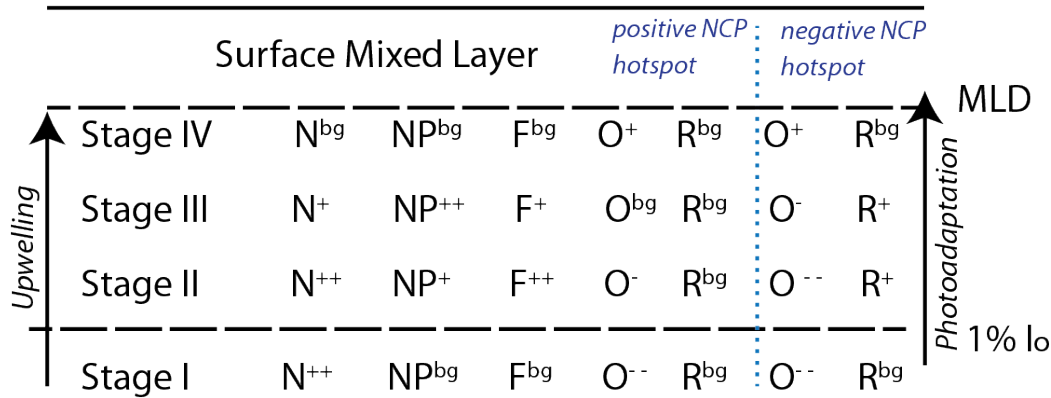
Fig. 5. (a) Schematic of a conceptual model which potentially explains the generation of a submesoscale hotspot. The model contains a nutrient (N), new production (NP), fluorescence (F), oxygen (O) and community respiration (R) resulting from a submesoscale upwelling event. Superscript "bg" indicates background conditions, whereas "+" and "-" signs indicate increasingly positive and negative anomalies, respectively. When the model is assembled from first principles, an autotrophic response to hotspots is expected, resulting in ΔO_2 ("Postive NCP column"). Negative ΔO_2 hotspots can be explained by either source waters not on the transect or by a modified model where respiration changes in magnitude during the upwelling event, shown in the last two columns ("Negative NCP"). . Depths of the mixed layer (MLD) and euphotic zone ($1\%\ I_0$) are depicted as dotted lines; the ocean surface is the bold line. (b) Schematic of effect on downwelling on fluorescence (F) and oxygen (O) with the dashed line showing the profile after downwelling and the solid line showing it before. Red horizontal arrows depict the positive O anomaly and negative F anomaly that results from donwelling. (c) Schematic illustrating that the stages depicted in part (a) of this figure can be diagnosed in the VPR-II data by considering the sign of F' and O' where primed quantities refer to the measured minus the average quantity on a given depth horizon (i.e. 1 m depth-averaged bin).
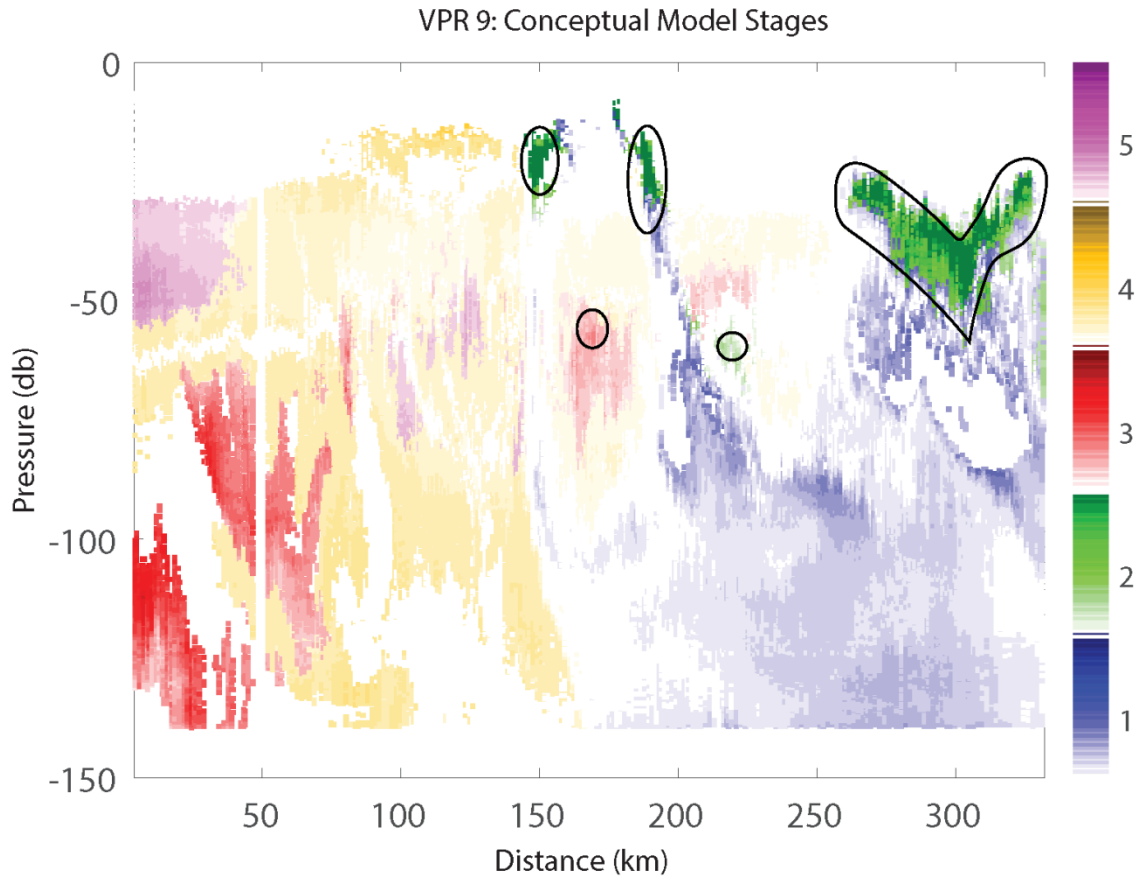
Fig. 6. The stages of the conceptual model, as diagnosed by O' and F', for VPR transect #9 . The black circles denote the locations of the hotspots shown in Fig. 1 and 2. As shown here, almost all hotspots in all the transects appear to be stage 2. Often, the progression from stage 1 to stage 2 is observed but rarely is the progression from stage 2 to stage 3 observed. Stage 3 is apparent in many of the tows, but not in the hotspots.

1
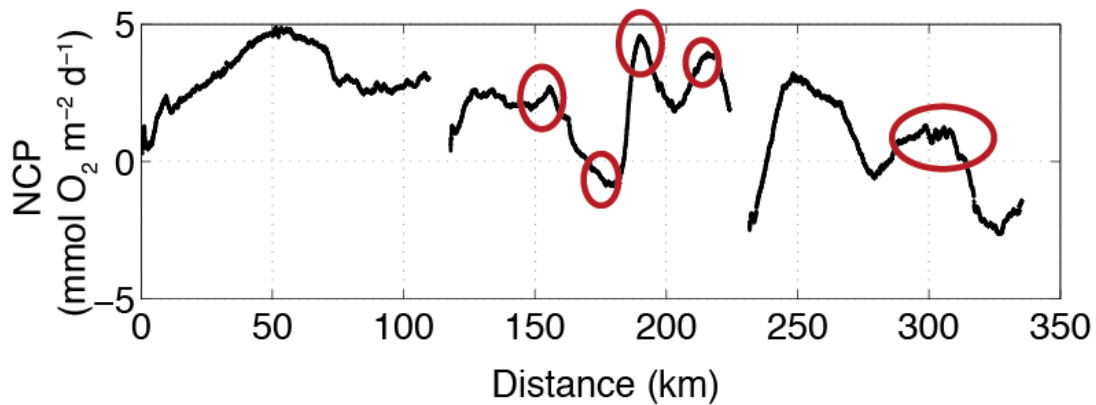
2

3   Fig. 7. Rates of Net Community Production (NCP) in the mixed layer as determined by O_2/Ar
4   measured by a shipboard equilibrator inlet mass spectrometer for VPR transect #9 (VPR data for
5   this transect shown in Fig. 2). Note that many of the peaks in NCP (circled in red) are visible as
6   hotspots in the VPR record. However, other peaks in NCP do not correspond to hotspots, though
7   they may be remnants of older hotspots since the O_2/Ar approach gives a weighted average of
8   productivity over approximately the past week.

9

10

11

12

Supplemental Material for

Submesoscale Hotspots of Productivity and Respiration: Insights from High-Resolution Oxygen and Fluorescence Sections

Rachel H. R. Stanley[1]*, Dennis J. McGillicuddy, Jr.[2], Zoe O. Sandwith[2], and Haley M. Pleskow[1]

[1] Wellesley College, 106 Central St. Wellesley, MA 02480

[2] Woods Hole Oceanographic Institution, 360 Woods Hole Rd., Woods Hole, MA USA 02543

* corresponding author: rachel.stanley@wellesley.edu, 001-781-283-3122

The supplementary material includes a table of latitudes and longitudes corresponding to the tows (Table S1) and plots of temperature, salinity, oxygen, fluorescence, and oxygen and fluorescence anomalies for all the VPR transects (Fig. S1 to S14) other than VPR #9 which is used as a case-study and thus appears in the main text. Additionally, the supplemental material describes a decorrelation length scale analysis and provides a figures of vertical and horizontal decorrelation length scales (Fig. S15) . It also includes a figure containing velocity vectors based on ADCP data, with the vectors superimposed on ADT contours (Fig. S16).

Decorrelation Length Scales

In order to gain more information on the spatial scales of the properties in our system, we calculated the decorrelation length scale (DLS) of oxygen, fluorescence, temperature and salinity in the VPR transects. We did this in both the vertical and horizontal directions.

For the vertical decorrelation length scales, we collapsed the VPR transects onto a series of profiles (i.e. the tow is actually a diagonal – a profile taken over a ~1 km spacing and we simply made it a single vertical profile, as if it were taken in exactly the same location). For each profile that contained a hotspot (based on identification hotspots as was done elsewhere in this paper), we calculated the DLS, by calculating an empirical semivariogram of the data (using matlab function variogram.m) and then using the range of a spherical fit to the semivariogram as a measure of the scale at which the decorrelation is zero (using matlab function variogramfit.m). We also calculated the DLS by calculating the length scale at which the autocorrelation of a property first crosses zero but since we needed to use the semivariogram method for our horizontal tows (due to different spacing between data points on density surfaces) we used the semivariogram method for the vertical tows too.   We calculated the average vertical DLS for each tow and then plotted the vertical DLS for oxygen, fluorescence, and salinity vs. vertical DLS for temperature (Fig. S15) in order to highlight how the other properties' DLS compares to that of temperature.

The average vertical decorrelation scale (Fig. S15) is usually larger for temperature than for fluorescence, suggesting that in the vertical direction, the variations in fluorescence are less tied to the surrounding water than temperature variations are. However, the large standard deviations on the average DLS for each tow (shown by errorbars in Fig S15a) make the

differences between DLS of the various properties insignificant. The average vertical DLS for oxygen are sometimes greater than and sometimes smaller than that of temperature when calculated using the semivariogram method and are consistently smaller than temperature when calculated using the autocorrelation zero crossing method (not shown). It is interesting that using both methods, the oxygen vertical DLS is longer than the fluorescent one, even though visually the hotspots we see are both in fluorescence and oxygen. In general, the decrease in vertical DLS for fluorescence and oxygen supports the idea that these variables are more patchy than temperature and that the hotspots are not simply a result of physical transport of water. The tendency for fluorescence to be more patchy than temperature is well established (Denman, 1976; Mackas et al., 1985; Pingree et al., 1975; Steele, 1978). Fewer studies exist comparing patchiness in oxygen and fluorescence, with some suggesting those two variables have similar patchiness and others that oxygen is more patchy than temperature   (Estapa et al., 2015). The DLS analysis, however, does not just reflect the hotspots but also incorporates data elsewhere in the profiles. Indeed the DLS are much longer than the spatial extent of the hotspots (i.e. vertical extend is ~10 m or less of many of the hotspots) suggesting the DLS may be giving background information on variability rather than specifically on hotspots.

To quantify the lateral variability of the hotspots, we calculated horizontal DLS along density surfaces. In particular, we used density surfaces only where hotspots were located. We then used the semivariogram method described above to calculate the distance at which data were no longer related and calculated averages of DLS for each transect. As before, we plotted the DLS for fluorescence, oxygen and temperature vs. DLS for temperature (Fig. S15b). Not surprisingly, since we were doing the calculations along density surfaces, the DLS for salinity is very similar to that of temperature in all cases. In the horizontal direction, DLS for oxygen are much smaller

than DLS for fluorescence, reflecting more horizontal patchiness in oxygen than in fluorescence, which is surprisingly different than the conclusions in the vertical direction. Once again, however, this conclusion is limited because of the large standard deviations of the DLS along a tow (shown by the large errorbars). Even though we selected density surfaces that had hotspots on them, the DLS may be reflecting the entire density surface rather than just the hotspot ; the values are larger than the width of the hotspot and are more reflective of the spaces inbetween hotspots. Additionally, density surfaces may not be appropriate for fluorescence, which responds strongly to light and thus is a property for which depth matters more than density. Autocorrelation across horizontal slices in depth space, rather than density space (not shown), does indeed show a slight decrease in decorrelation length scales for fluorescence compared with temperature and salinity, though again the differences are not statistically significant.

Figure Captions for Supplemental Material:

Fig. S1 to 14: Data from other VPR transects (VPR transects 1 to 16, not including VPR transect 9 which is shown in Fig. 2 or VPR transect 13 which was a failed tow) presented in same way as Fig. 2. (a) potential temperature in deg C, (b) salinity (c) fluorescence (relative fluorescent units), (d) oxygen concentration in μmol L^{-1}, (e) fluorescence anomaly (relative fluorescence units), and (f) oxygen concentration anomaly in units of μmol L^{-1}. The labels next to the color bar reflect the minimum and maximum values of that property on that particular transect. The gray circles reflect the location of the hotspots marked in Fig. 1. White lines represent isopycnal surfaces. Data are not contoured – rather each pixel represents a data point collected by sensors on the VPR-II.

Fig. S15. (a) Vertical and (b) horizontal decorrelation length scales for the data, averaged on each transect, and calculated using the semivariogram method as described in the text. Horizontal decorrelation length scales were calculated along density surfaces containing hotspots and vertical decorrelation length scales were calculated on profiles containing hotspots. Error

bars reflect the standard deviation of the decorrelation length scales within a transect and are evidence for the large variability in decorrelation length scales across a given transect.

Fig. S16. Surface water velocity vectors, from ADCP data, along the cruise track superimposed on contours of absolute dynamic topography. Northern and southern sections are similar as to those presented in Fig. 1. The velocity vectors suggest that most water in the hotspots did not come from the tow itself.

References for Supplemental Material

Denman, K.L., 1976. Covariability of chlorophyll and temperature in the sea. Deep Sea Research 23, 539-550.

Estapa, M.L., Siegel, D.A., Buesseler, K.O., Stanley, R.H.R., Lomas, M.W., Nelson, N.B., 2015. Decoupling of net community and export production on submesoscales in the Sargasso Sea. Global Biogeochem. Cycles 29, 1266-1282.

Mackas, D.L., Denman, K.L., Abbott, M.R., 1985. Plankton patchiness: biology in the physical vernacular. Bull. Mar. Sci. 37, 652-674.

Pingree, R.D., Pugh, P.R., Holligan, P.M., Forster, G.R., 1975. Summer phytoplankton blooms and red tides along tidal fronts in the approaches to the English Channel. Nature 258, 672-677.

Steele, J.H., 1978. Spatial pattern in plankton communities. Plenum Press, New York.

Table S1. Initial and final latitude and longitude for the VPR-II tows.

Tow #	Initial latitude	Final latitude	Initial longitude	Final longitude
1	31.63	25.50	-64.16	-66.29
2	25.49	22.18	-66.21	-66.00
3	22.18	20.01	-65.93	-63.35
4	19.99	17.91	-63.25	-60.98
5	17.93	18.22	-60.94	-61.25
6	18.23	15.50	-61.28	-59.88
7	15.52	14.90	-59.76	-57.89
8	14.89	15.10	-57.83	-57.46
9	15.13	12.30	-57.47	-56.42
10	12.37	13.95	-56.32	-54.58
11	13.92	15.76	-54.54	-52.77
12	15.79	15.60	-52.76	-53.00
14	15.60	15.60	-53.06	-53.01
15	15.59	16.48	-53.02	-55.60
16	16.45	14.66	-55.43	-57.54

Figures S. 1 to S14: Data from other VPR transects (VPR transects 1 to 16, not including 9 which is shown in Fig. 2 or 13 which was a failed tow) presented in same way as Fig. 2. (a) potential temperature in deg C, (b) salinity in psu, (c) fluorescence (relative fluorescent units), (d) oxygen concentration in µmol L^{-1}, (e) fluorescence anomaly (relative fluorescence units), and (f) oxygen concentration anomaly in units of µmol L^{-1}. The labels next to the color bar reflect the minimum and maximum values of that property on the tow. The gray circles reflect the location of the hotspots marked in Fig. 1. White lines represent isopycnal surfaces. Data are not contoured – rather each pixel represents a data point collected by sensors on the VPR-II. These figures are in the attached pdf.
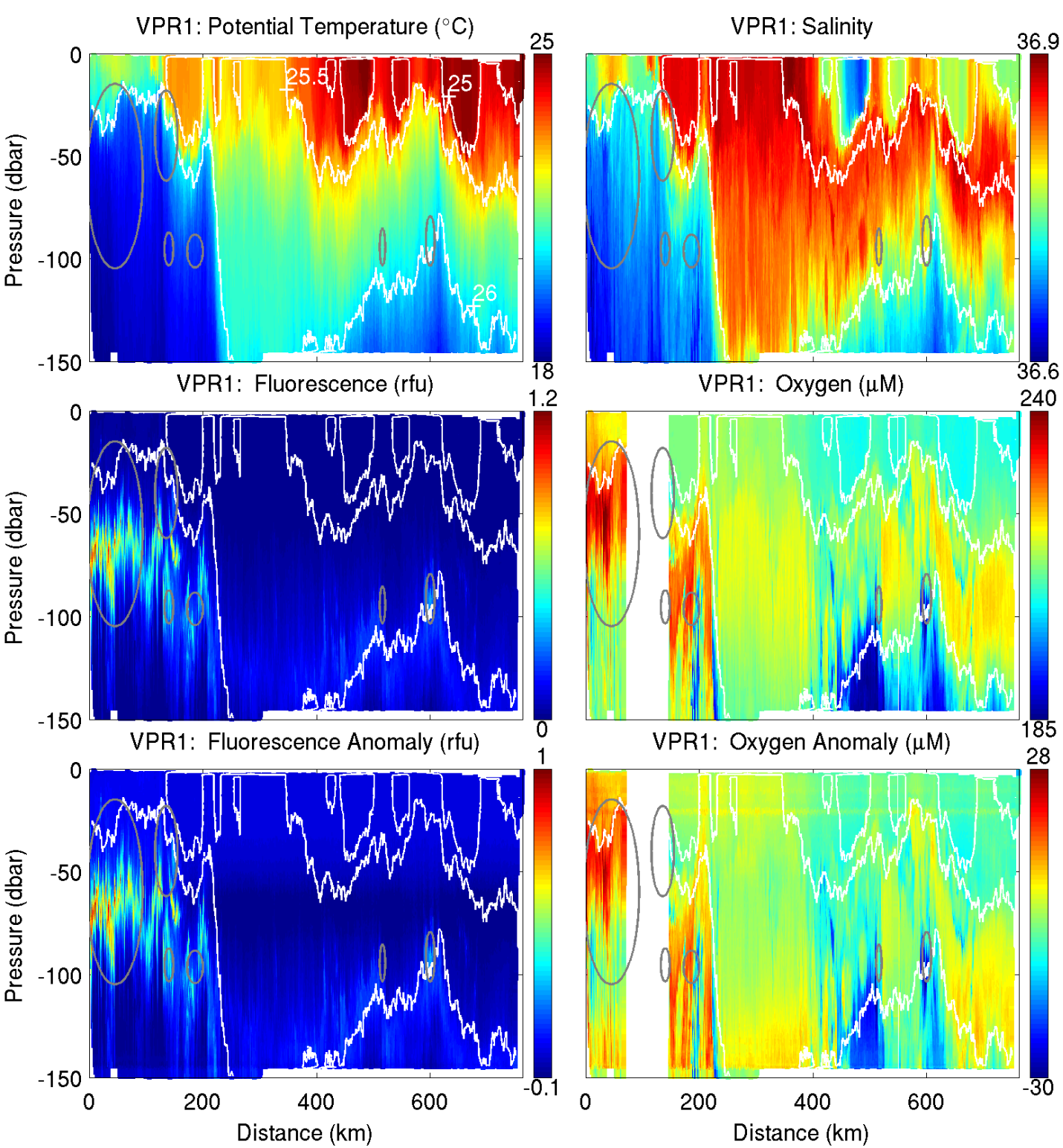
Figure S1
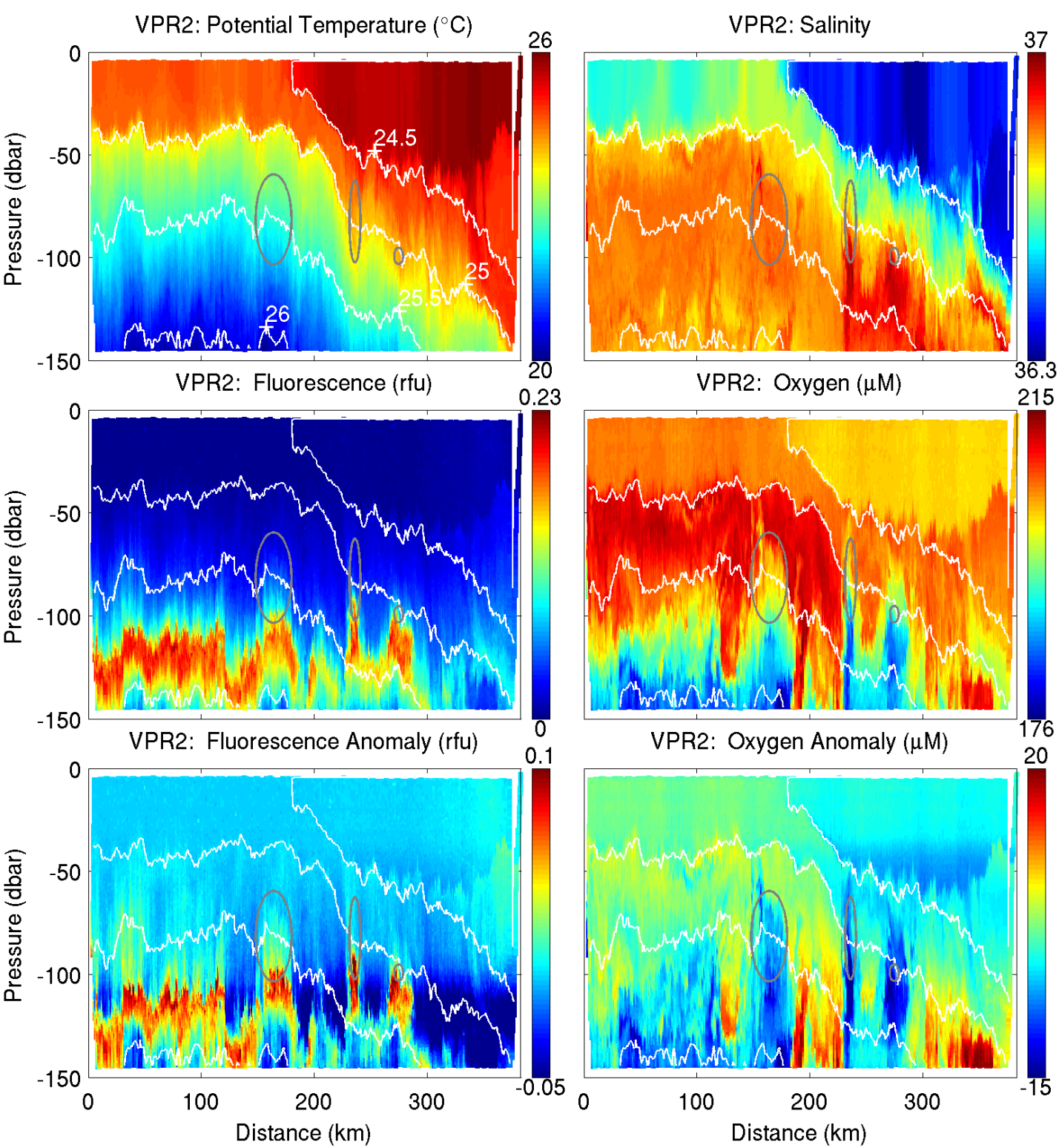
Figure S2
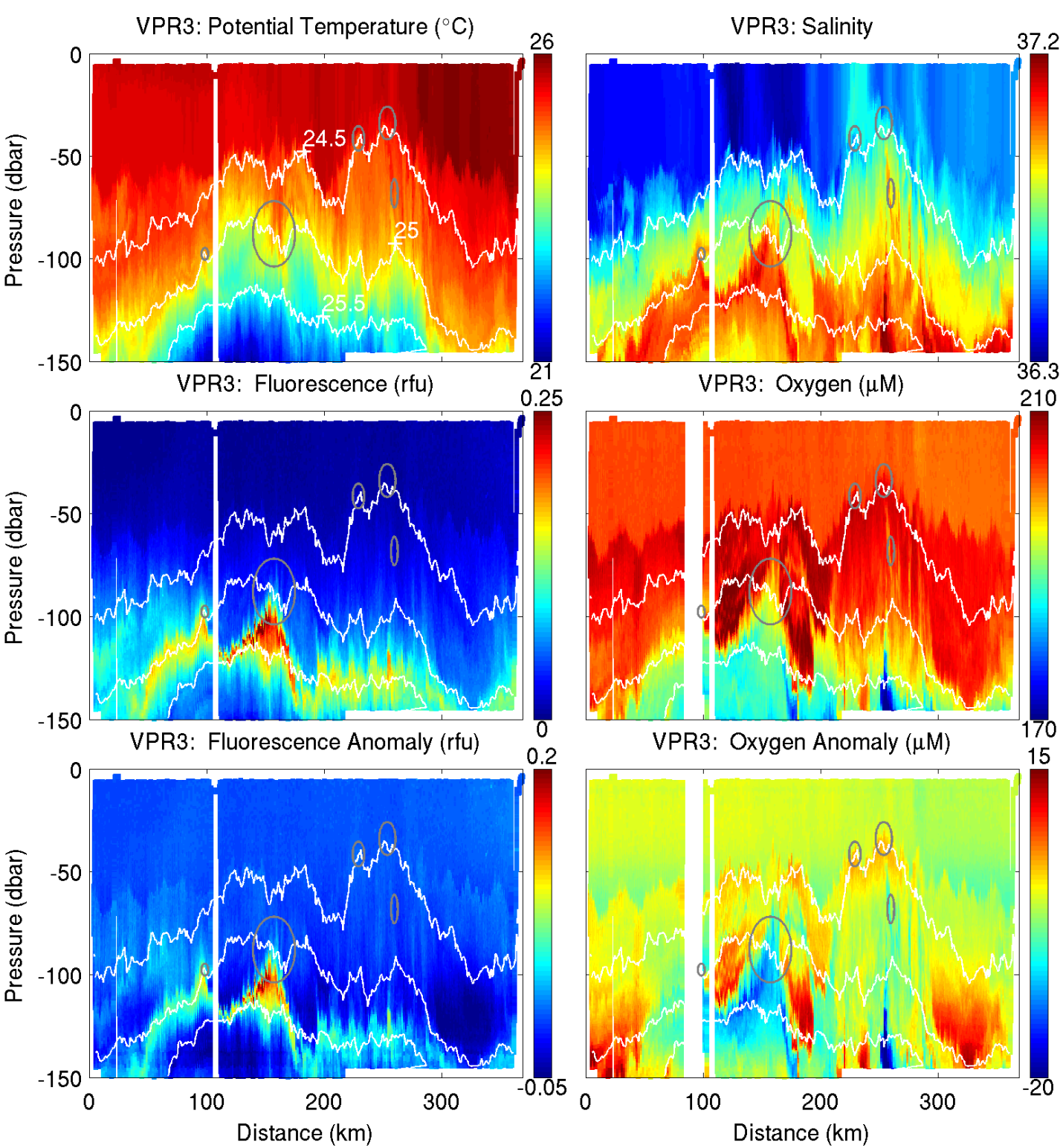
Figure S3
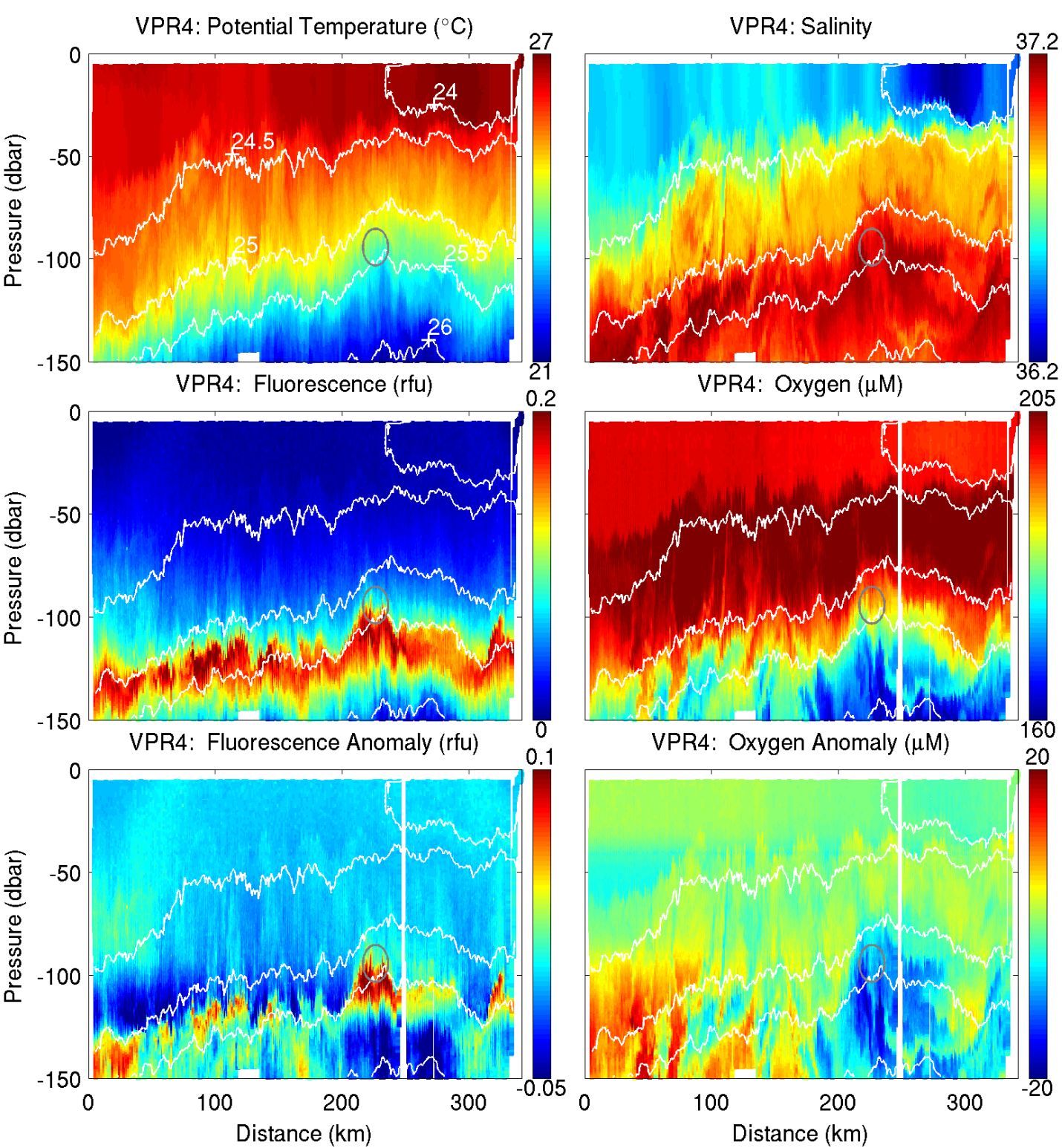
Figure S4
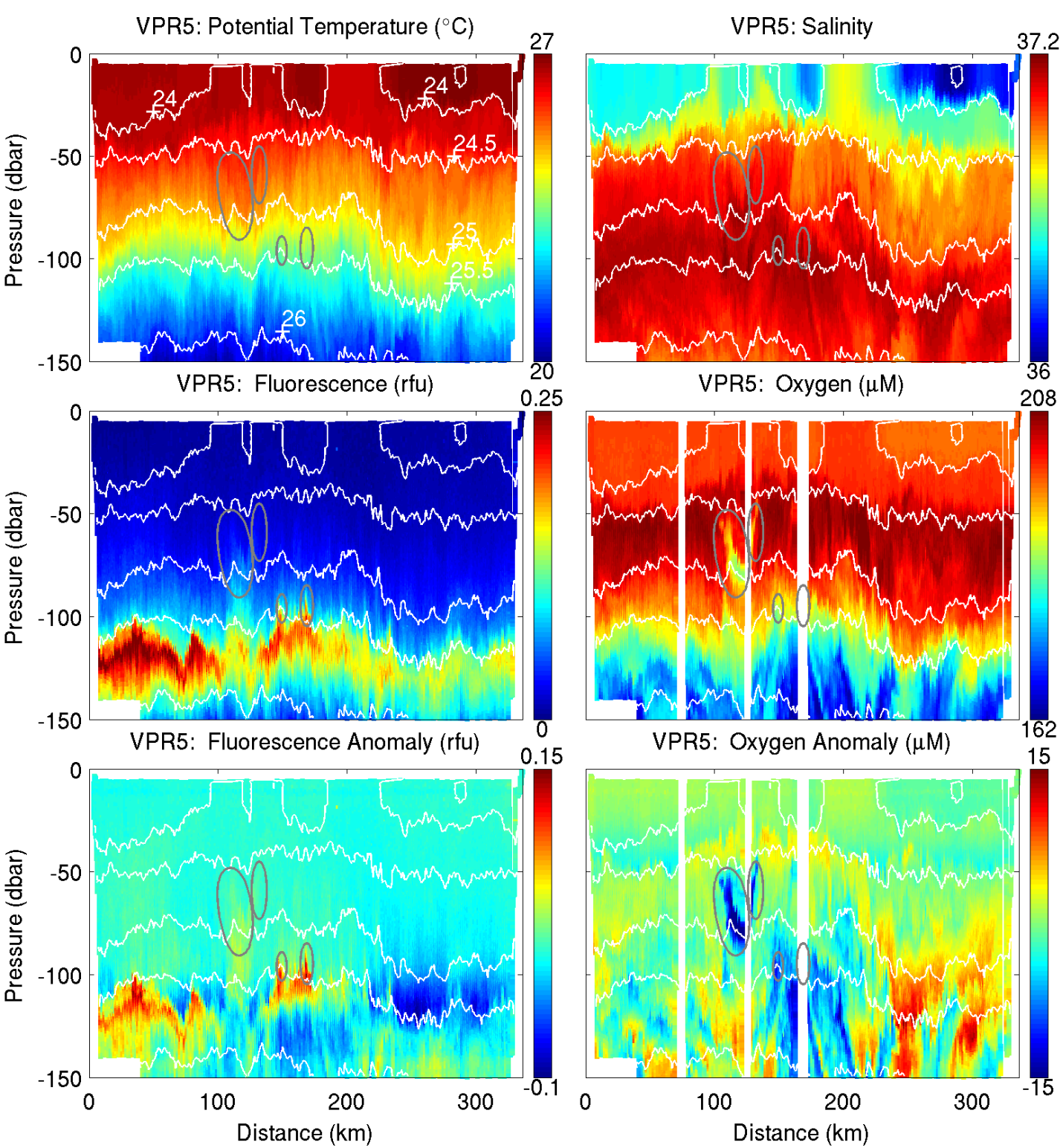
Figure S5
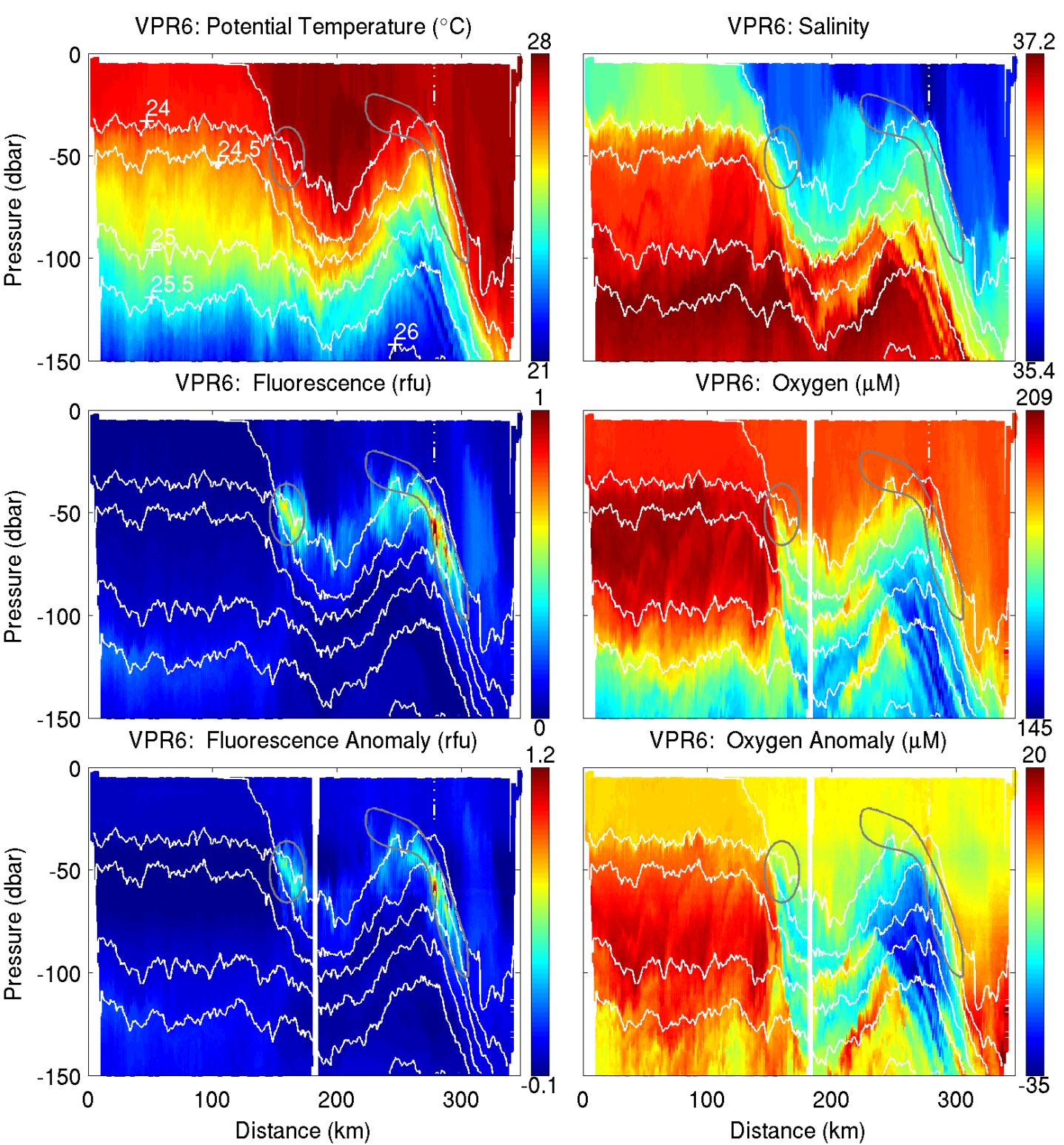
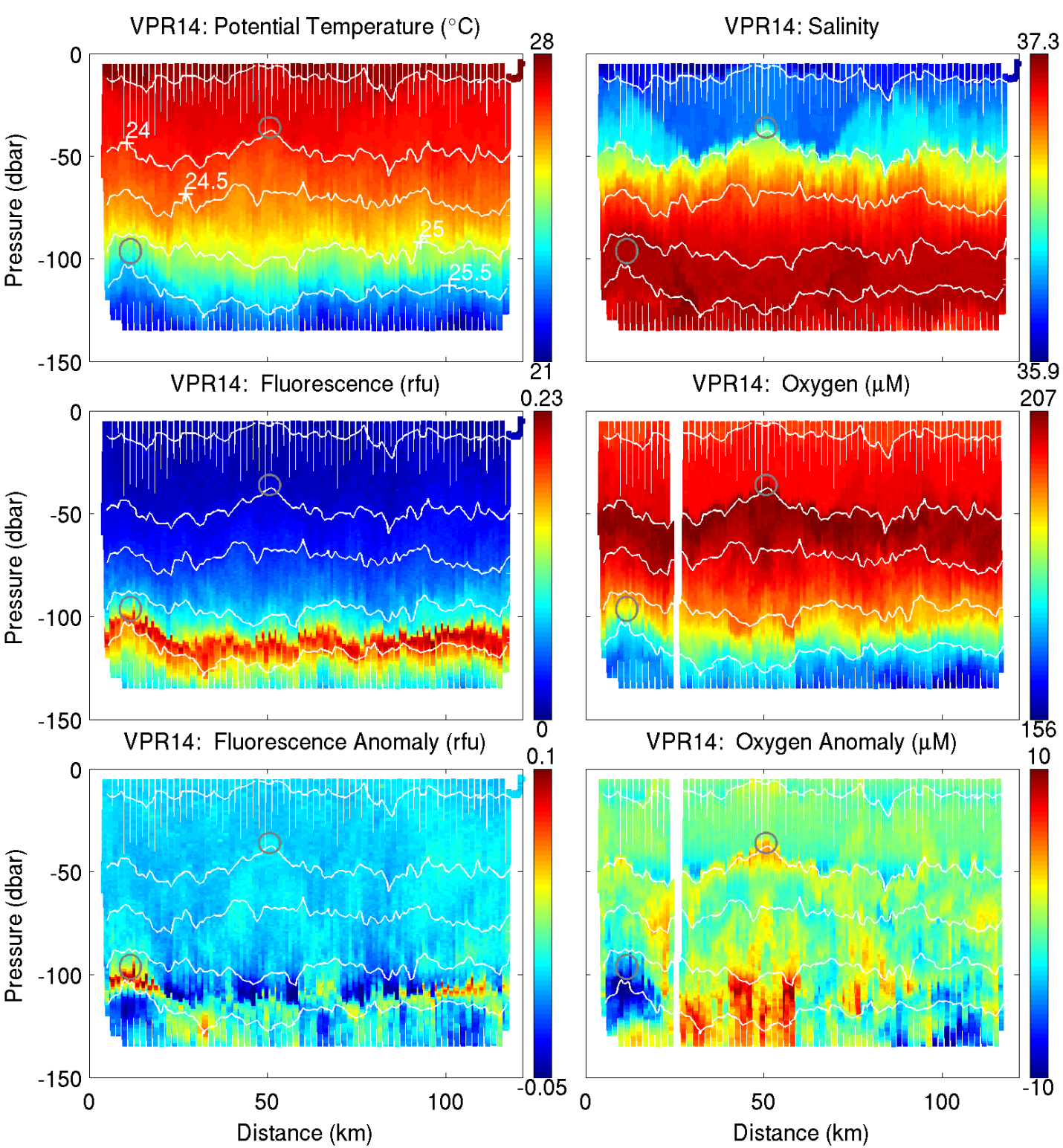Figure S6
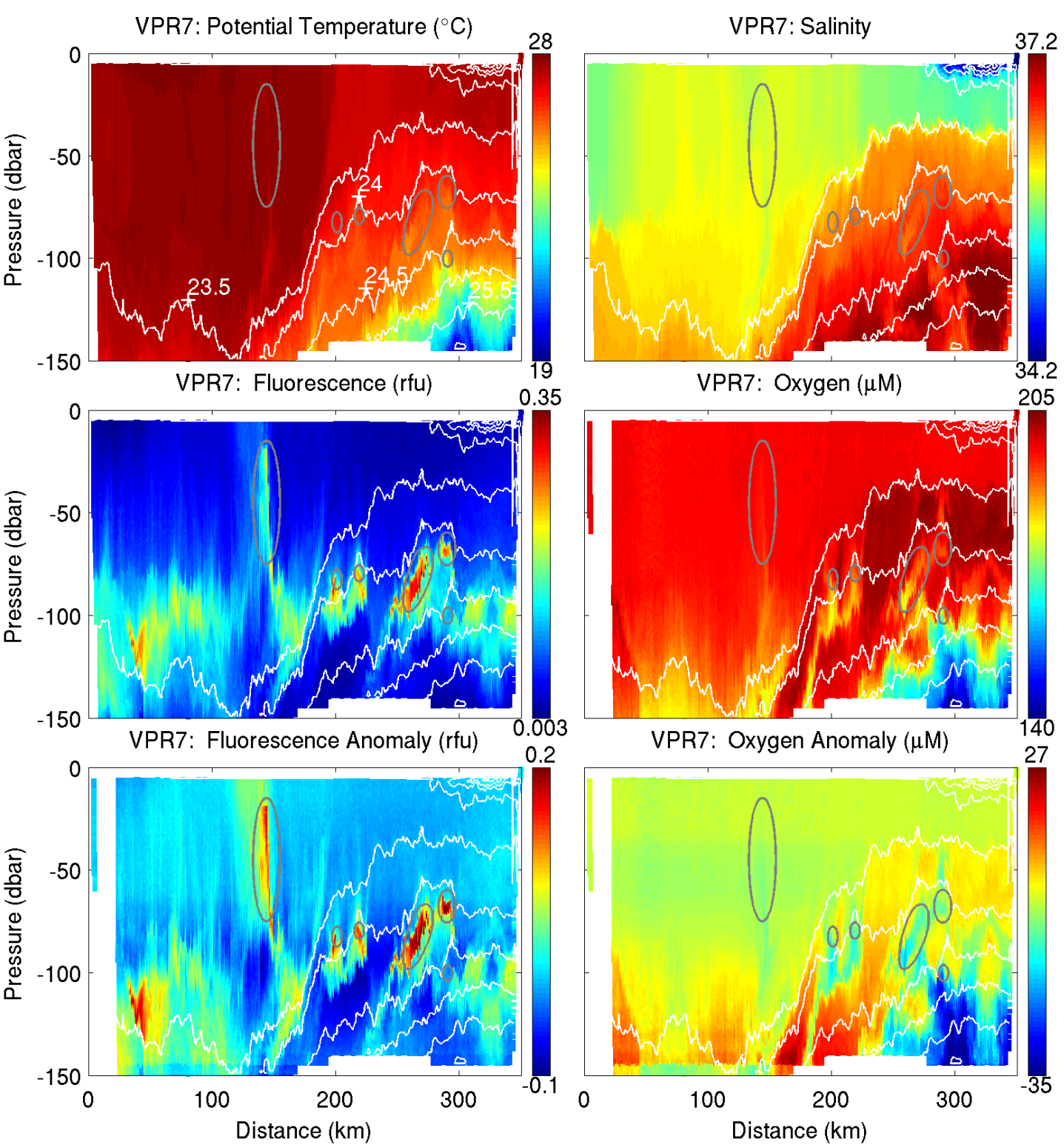
Figure S7
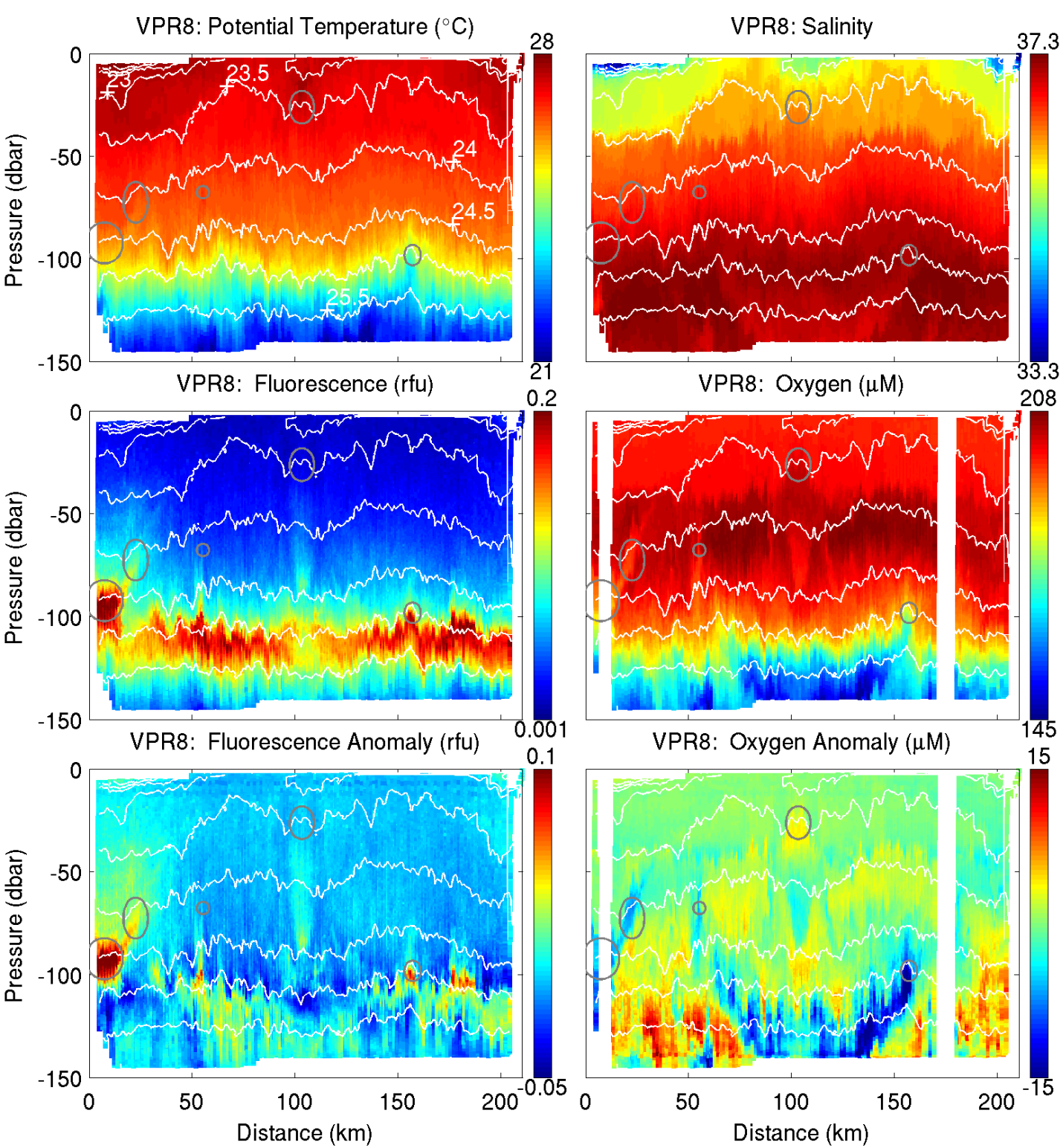
Figure S8
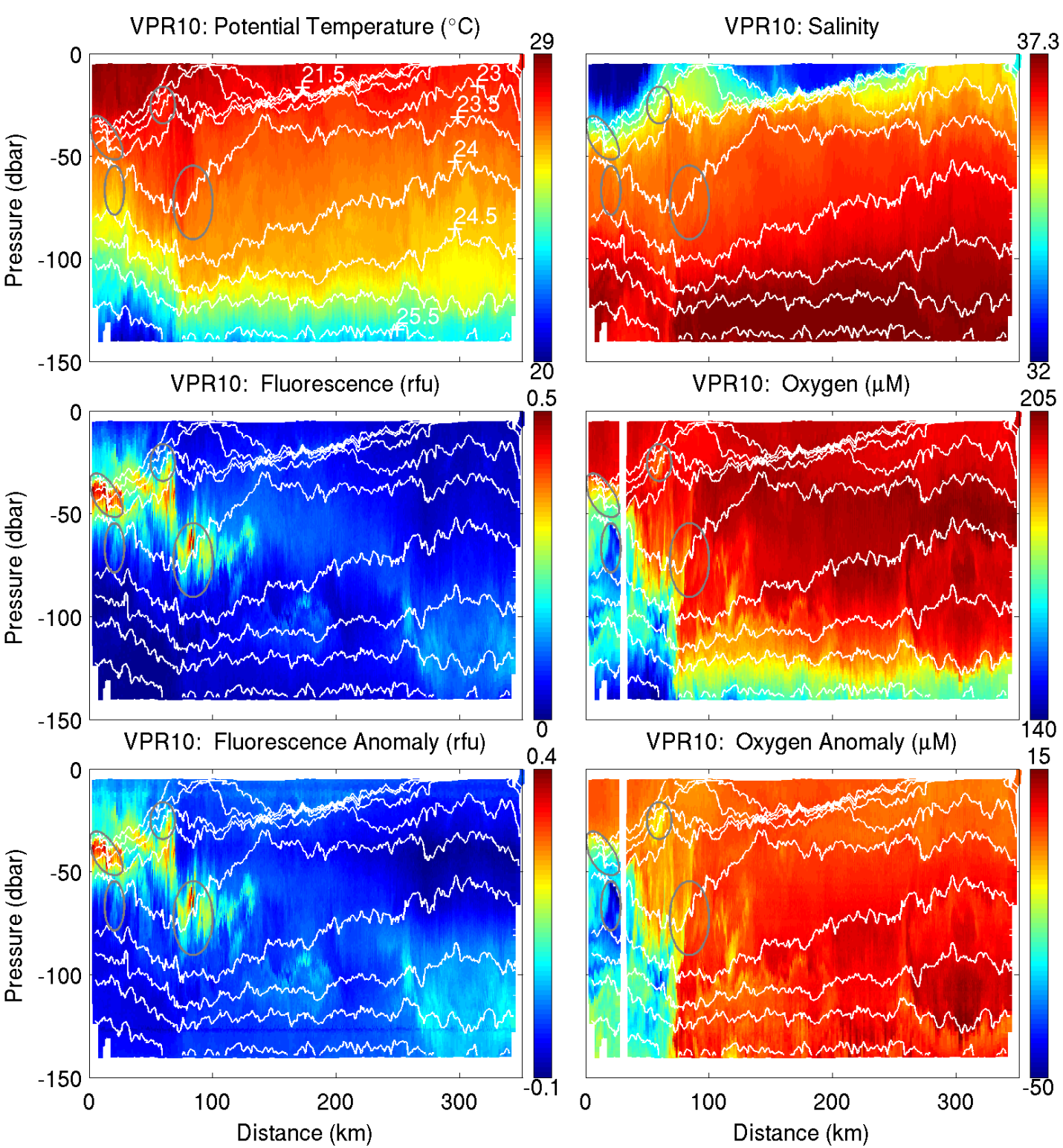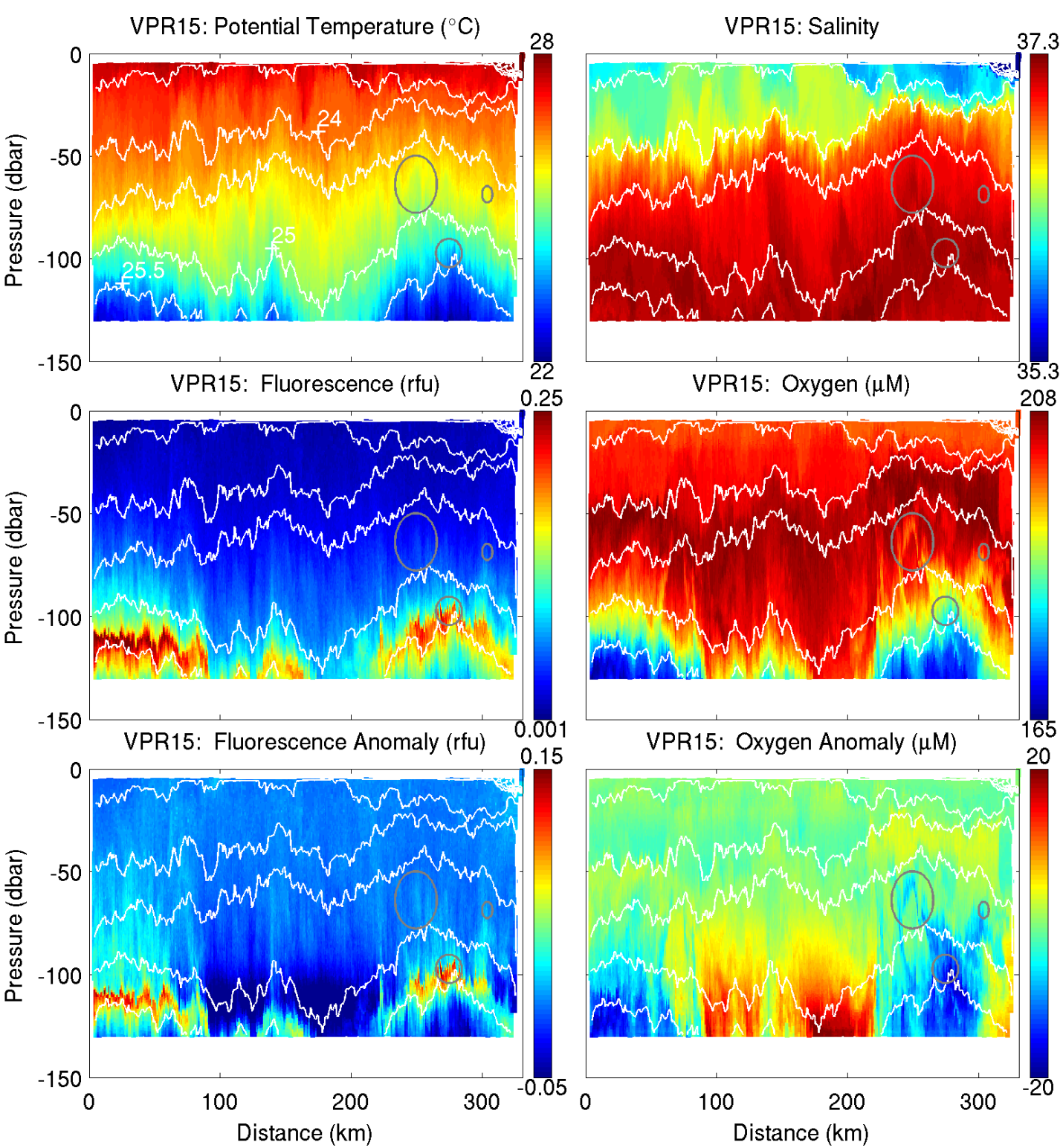
Figure S9
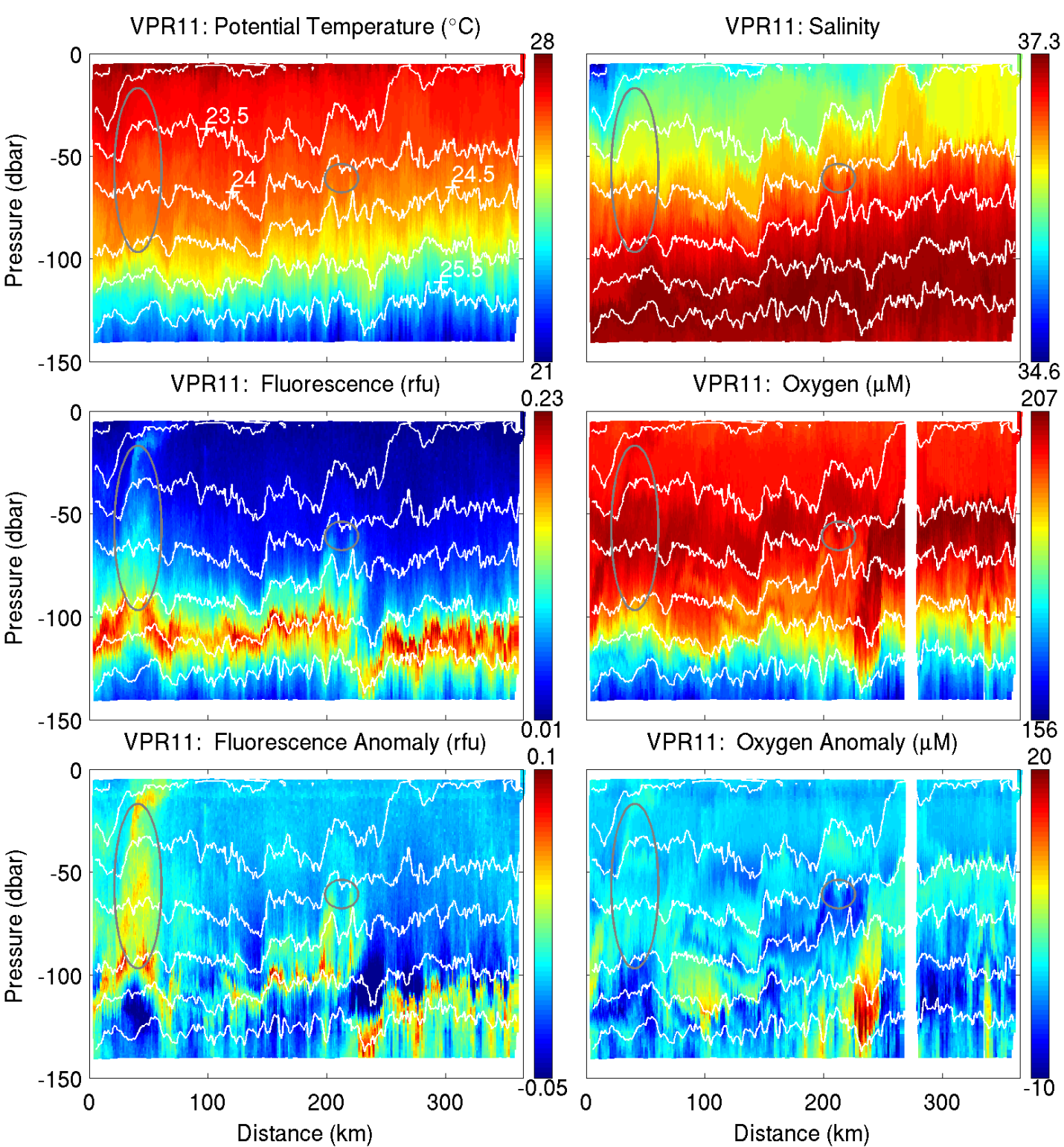
Figure S10
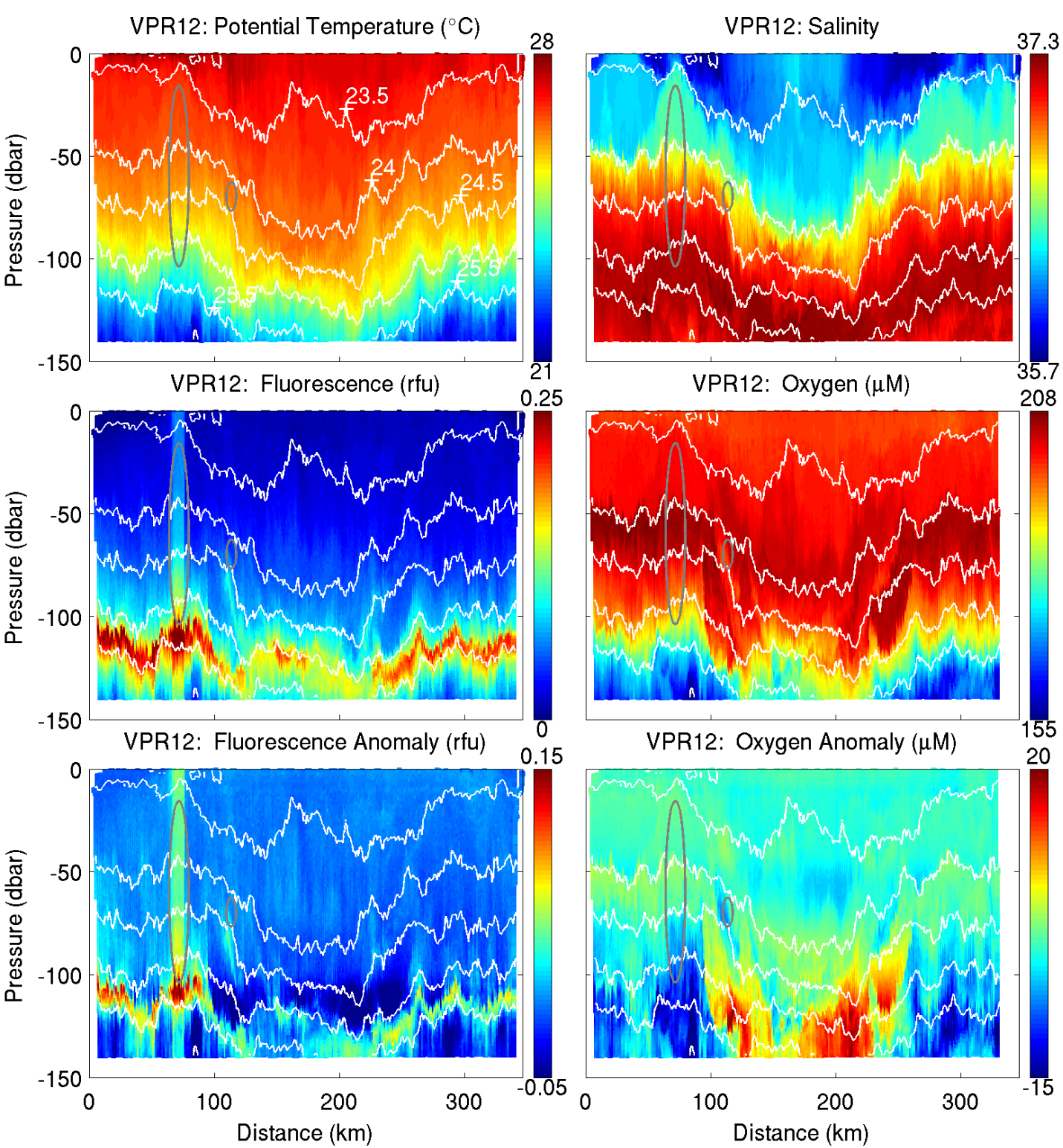
Figure S11
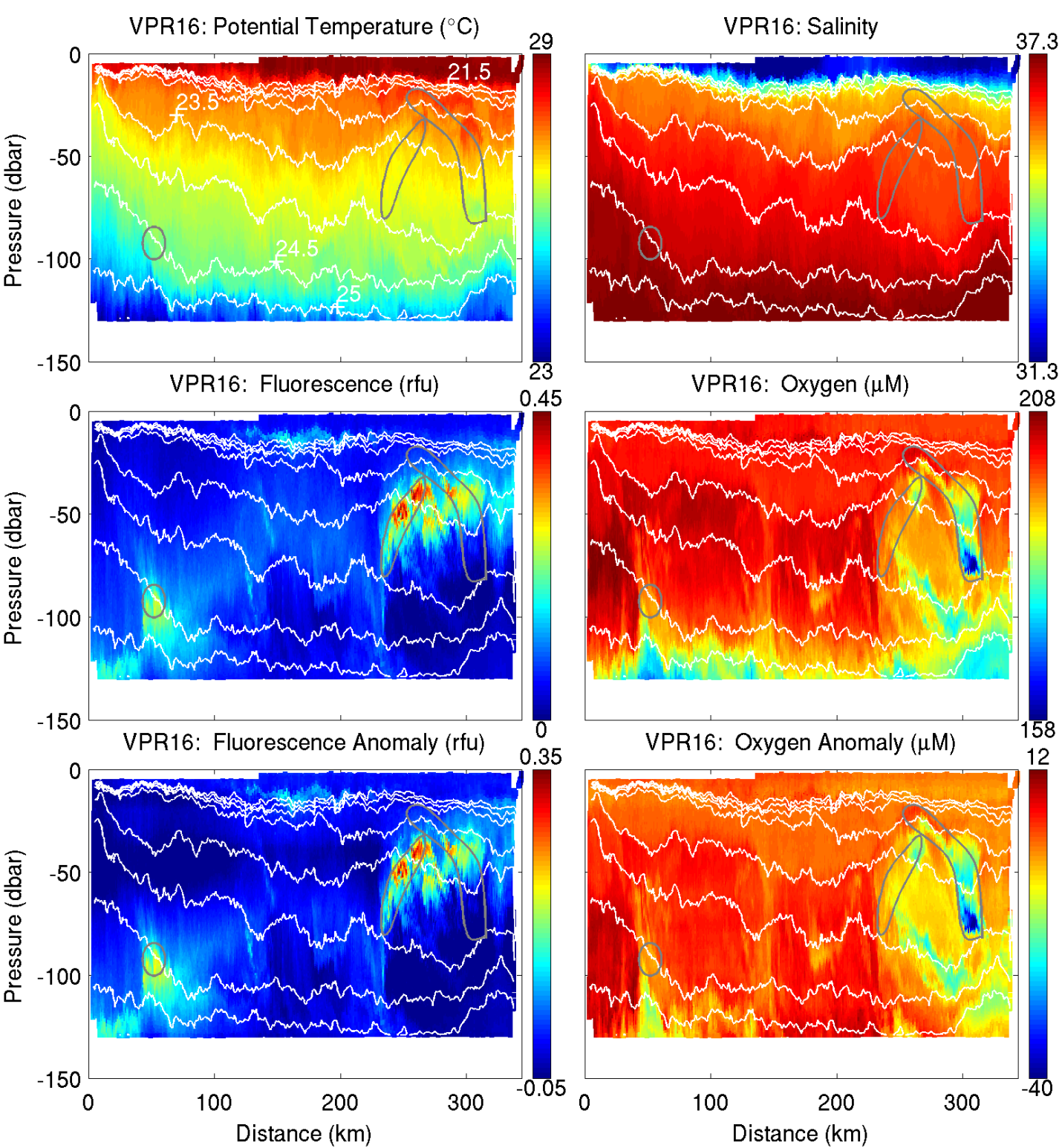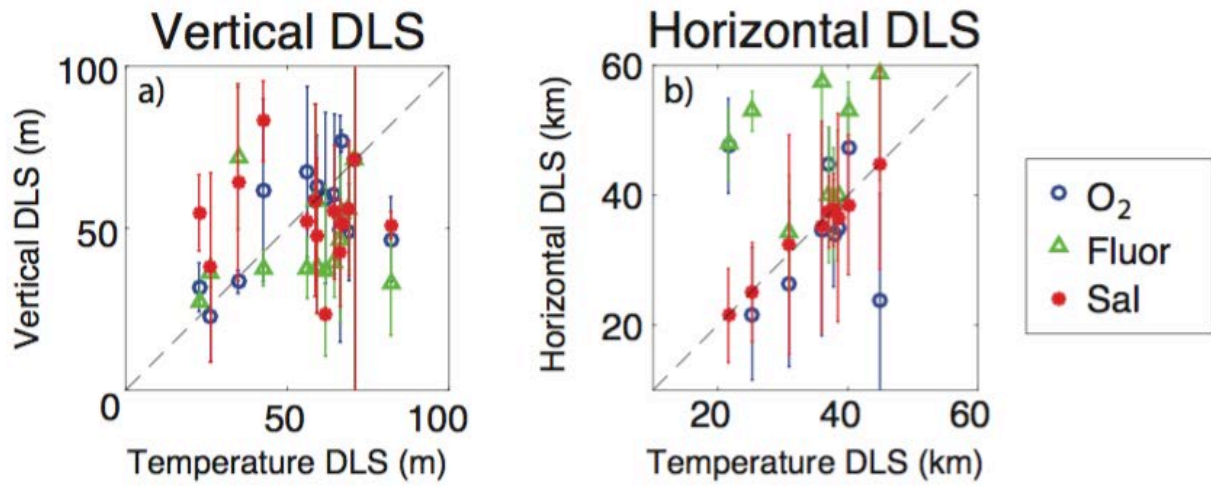
Figure S12

Figure S13

Figure S14

Figure S15

Fig. S15. (a) Vertical and (b) horizontal decorrelation length scales for the data, averaged by tow, and calculated using the semivariogram method as described in the text. Horizontal decorrelation length scales were calculated along density surfaces containing hotspots and vertical decorrelation length scales were calculated on profiles containing hotspots. Error bars reflect the standard deviation of the decorrelation length scales within a tow and show the large variability across a given tow.
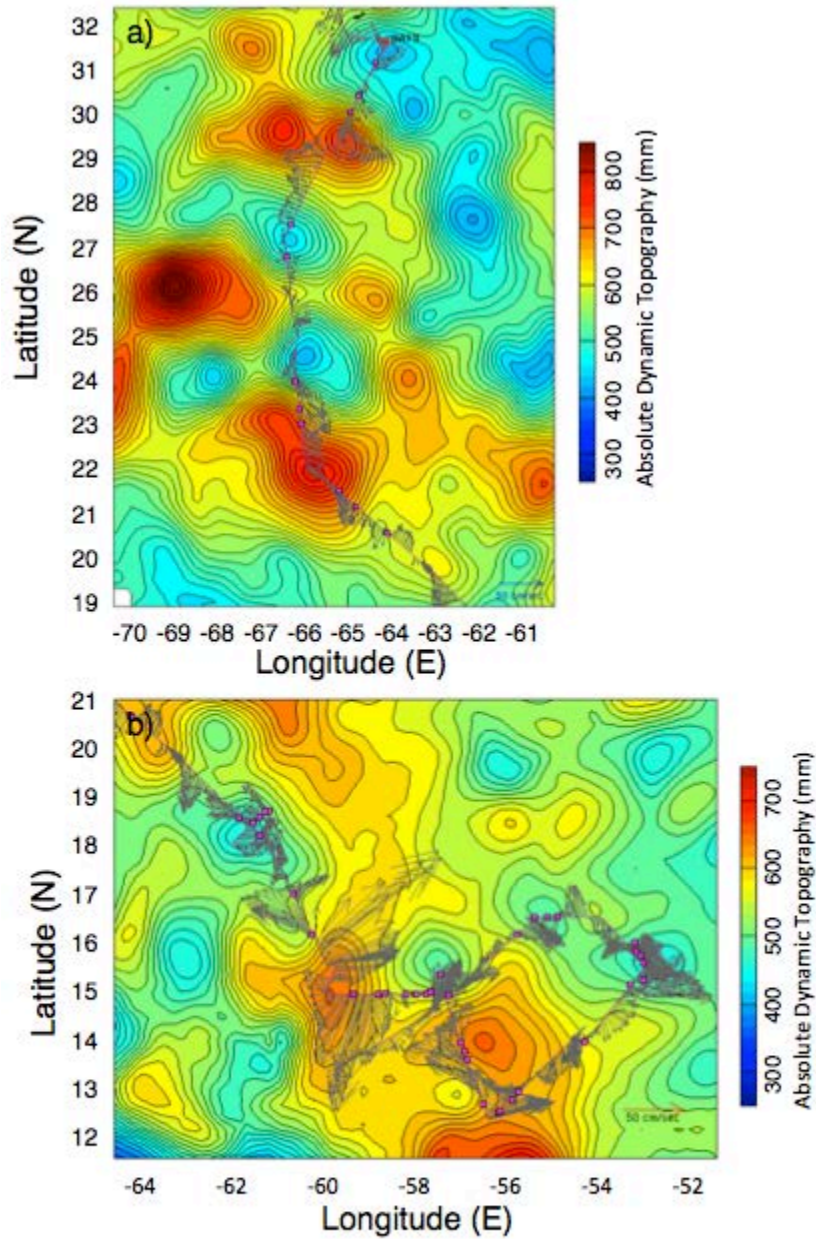
Figure S16

Fig. S16. Surface water velocity vectors, from ADCP data, along the cruise track superimposed on contours of absolute dynamic topography. Northern and southern sections are similar as to those presented in Fig. 1. The velocity vectors suggest that most water in the hotspots did not come from the tow itself.